*J. Fluid Mech.* (2023), *vol*. 964, A15, doi:10.1017/jfm.2023.356

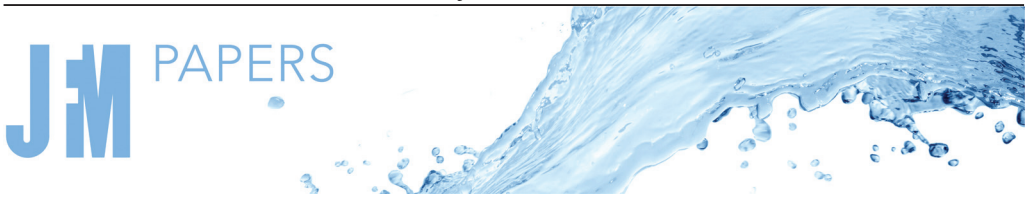

# Linear-model-based study of the coupling between velocity and temperature fields in compressible turbulent channel flows

**Cheng Cheng**[1] **and Lin Fu**[1,2,3,†]

[1]Department of Mechanical and Aerospace Engineering, The Hong Kong University of Science and Technology, Clear Water Bay, Kowloon, Hong Kong

[2]Department of Mathematics, The Hong Kong University of Science and Technology, Clear Water Bay, Kowloon, Hong Kong

[3]HKUST Shenzhen-Hong Kong Collaborative Innovation Research Institute, Futian, Shenzhen 518048, PR China

(Received 9 January 2023; revised 20 March 2023; accepted 22 April 2023)

It is generally believed that the temperature and the velocity fields are highly coupled in compressible wall-bounded turbulence. In the present study, we employ a linear model, i.e. the two-dimensional spectral linear stochastic estimation (SLSE), to study this coupling from the perspective of the multi-scale energy-containing eddies. Particular attention is paid to the relevant statistical characteristics of the temperature field. The connections of the two fields are found to be varied with the wall-normal position in the boundary layer. In a nutshell, their entanglement is strongest in the near-wall region, and only the extreme thermal events cannot be captured by SLSE. In the logarithmic region, only the scales that correspond to the attached eddies and the very large-scale motions (VLSMs) are firmly coupled. The near-wall footprints of the former are organized in an additive manner and fulfil the predictions of the celebrated attached-eddy model. In the outer region, the two fields are linearly coupled only at the scales corresponding to VLSMs. These findings are demonstrated to be insensitive to the Mach number effects and ascribed to the similarity between the momentum and the heat transfer in compressible wall turbulence. It is also shown that it is the Reynolds number rather than Mach number that acts as a key similarity parameter in constructing their coupling. The framework built in the present study may pave a way for investigating the multi-physics coupling in turbulence, and reinforcing our analysing and modelling capability to the interrelated problems.

**Key words:** turbulent boundary layers, turbulence modelling, compressible boundary layers

† Email address for correspondence: linfu@ust.hk

## 1. Introduction

Multi-physics coupling is the typical aspect of turbulence, whereby different physical quantities interact with each other at broadband length scales. In incompressible turbulence, the coupling between the pressure and the velocity fields leads to the complex picture of the scale interactions (Tsuji, Marusic & Johansson 2016; Cho, Hwang & Choi 2018; Lee & Moser 2019). As for the wall-bounded turbulence with heat transfer, the most noteworthy one is the coupling between the temperature and the velocity fields. The existing studies reveal the two fields in many similarities, but differences as well (Antonia, Abe & Kawamura 2009; Pirozzoli & Bernardini 2011; Li *et al.* 2019; Cheng & Fu 2022*b*). A deep understanding about this process is of great practical significance. All in all, one persistent pursuit of high-speed aerodynamics is suppressing wall friction with controlled wall heat flux. Uncovering their intricate entanglement may allow us to develop the sophisticated flow control strategies.

As early as the 1960s, Morkovin (1962) derived the well-known strong Reynolds analogy (SRA) for the zero pressure-gradient compressible turbulent boundary layers with adiabatic wall condition. This original SRA takes the form of

$$\frac{\sqrt{\overline{T'^2}}/\bar{T}}{(\gamma-1)M^2\sqrt{\overline{u'^2}}/\bar{u}}=1, \tag{1.1}$$

where $\gamma$, $M$ denote the specific heat ratio and the local mean Mach number. Additionally, $T'$, $u'$ represent the temperature and the streamwise velocity fluctuations, respectively, and $\bar{T}$, $\bar{u}$ represent their mean counterparts. SRA is deduced based on some assumptions that are too ideal, thus, it has been discovered to have severe limitations in subsequent studies and several variants have been proposed by taking the wall heat flux into consideration (Cebeci & Smith 1976; Gaviglio 1987; Rubesin 1990; Huang, Coleman & Bradshaw 1995; Zhang *et al.* 2014). However, it undoubtedly underlines the fact that the temperature field is highly coupled with the velocity field in compressible wall turbulence. This crucial topic has also been inspected from the view of the coherent structures and the multi-scale eddies in follow-up works. For example, Pirozzoli & Bernardini (2011) reported that the temperature field in the inner layer of a supersonic turbulent boundary layer also exhibits a clear streaky pattern, qualitatively similar to that of the streamwise velocity fluctuations, whereas their similarities become less apparent in the outer region. This observation indicates that the coupling between the two fields is not set in stone in physical space. Its variation is also reflected by the correlations between $u'$ and $T'$ (denoted as $R_{u'T'}$) at different wall-normal heights in a boundary layer. Specifically, for compressible turbulent channel flows, $R_{u'T'}$ reaches its maximum value in the near-wall region, and gradually diminishes as the wall-normal position increases (Coleman, Kim & Moser 1995; Brun *et al.* 2008; Gerolymos & Vallet 2014) (the reader can also refer to figure 2(*c*) of the present work). Yu & Xu (2021) inspected the one-dimensional linear coherence spectra of $u'$ and $T'$ in hypersonic turbulent channel flows, and found their coupling is scale-dependent and only strong at large scales. Though these pioneering studies shed light on some essential features of their coupling, some meaningful details are still unknown, e.g. its relationship with the energy-containing motions and the turbulence intensity that results from this coupling, etc. The motivations of the current study are to clarify them, and reinforce our analysing and modelling capability of the $u$–$T$ coupling in compressible wall turbulence (Fu *et al.* 2021; Fu, Bose & Moin 2022).

One piece of information is noteworthy regarding the relationship between the energy-containing motions and the $u$–$T$ coupling, which is one of the concerns

raised above. Pirozzoli & Bernardini (2011) recognized that the $T'$ motions populating the logarithmic and the outer regions in supersonic boundary layers would exert footprints on the near-wall region just like the $u'$ motions (Del Álamo & Jiménez 2003; Abe, Kawamura & Choi 2004*a*; Hutchins & Marusic 2007), though they are much weaker than the $u'$ counterparts. It is noted that the footprints of the $T'$ in the near-wall region are also reported to be existing in the incompressible turbulent channel flows with a passive temperature (Abe, Kawamura & Matsuo 2004*b*). The similarity between $u'$ and $T'$ suggests that the thermodynamic variable $T$ can also be categorized as a wall-attached quantity, and described by the celebrated attached eddy model (AEM). As is known to all, AEM is a conceptual model which illustrates the energy-containing motions residing in the logarithmic region in incompressible wall turbulence (Townsend 1976; Perry & Chong 1982). It conjectures that the logarithmic region is occupied by an array of self-similar energy-containing motions (or eddies) with their roots attached to the near-wall region. A growing body of evidence, which supports the theoretical predictions made with the AEM in incompressible wall-bounded turbulence, has emerged over the last two decades (Del Álamo *et al.* 2006; Lozano-Durán, Flores & Jiménez 2012; Hwang 2015; Hwang & Sung 2018; Lozano-Durán & Bae 2019; Cheng *et al.* 2020*b*; Hu, Yang & Zheng 2020). The reader can refer to Marusic & Monty (2019) for more details. Hence, investigating the $u$–$T$ coupling from the standpoint of AEM can not only clarify the energy-containing motions which are responsible for the coupling, but also broaden the applicability of AEM. Nearly all the previous studies on AEM treat $u'$, rather than $T'$, as the underpinning of the attached eddy. Additionally, the well-established analytical technologies developed in the AEM study (Baars, Hutchins & Marusic 2016; Baars & Marusic 2020; Cheng & Fu 2022*a*; Cheng, Shyy & Fu 2022) can also be generalized to cast light on the scale interactions engaging with the $T'$ motions in more complicated compressible wall turbulence. Some studies that have just been published on the temperature field in supersonic wall turbulence suggest that this research perspective is plausible. Yu *et al.* (2022) employed the proper orthogonal decomposition (POD) to identify the self-similar structures of the temperature fluctuations in a compressible channel flow. The statistical characteristics of some decomposed modes fulfil the AEM predictions. Yuan *et al.* (2022) adopted the three-dimensional clustering methodology to extract the wall-attached temperature structures in supersonic turbulent boundary layers. The conditional statistics of these structures are also consistent with the AEM descriptions. The authors of the present study also used the linear coherence spectrum to evaluate the geometrical characteristics of the self-similar $T'$ structures in subsonic/supersonic channel flows (Cheng & Fu 2022*b*). The streamwise/wall-normal aspect ratio of them is approximately 15.5, which resembles that of the $u'$ structures in incompressible boundary layers (Baars, Hutchins & Marusic 2017). These previous studies demonstrate that it is sensible to envision the temperature motions in the logarithmic region of compressible wall turbulence as underpinnings of the attached eddies. Are they accountable for the $u$–$T$ coupling? How do they impose influences on the near-wall small-scale flow? These questions still need to be answered.

The methodology employed in the present study is the linear model, i.e. the two-dimensional (2-D) spectral linear stochastic estimation (SLSE). In the 1970s, Adrian (1979) proposed that the prediction of the fluctuating velocity signals $u_i$ at $y_p$ (the predicted wall-normal position) from the measurements of the state-vector $\boldsymbol{u}$ at $y_m$ (the measured wall-normal position) can be obtained by Taylor-series expansion. It can be cast as

$$u_{ip}(y_p, t) = A_{ij}(y_m, y_p)u_{jm}(y_m, t) + B_{ijk}(y_m, y_p)u_{jm}(y_m, t)u_{km}(y_m, t) + \cdots, \qquad (1.2)$$

where $A_{ij}$ and $B_{ijk}$ are the second- and third-order two-point correlation tensors, respectively. The subscripts $m$ and $p$ stand for the measured and predicted physical quantities, and $i$, $j$, $k$ denote the components of the state-vector $\boldsymbol{u}$. For the linear stochastic estimation (LSE), only the first term on the right-hand side of (1.2) is taken into consideration. Over the years, the spectral version of LSE, namely SLSE, has been exploited as a potent tool to study the multi-scale structures in incompressible flows, such as the spectral contents of the attached eddies (Baars & Marusic 2020), the geometrical characteristics of the wall-attached structures (Baars *et al.* 2017; Baidya *et al.* 2019), the streamwise inclination angle of the attached eddies (Deshpande, Monty & Marusic 2019; Cheng *et al.* 2022), the prediction of the logarithmic-layer turbulence based on the wall quantities (Encinar & Jiménez 2019), and the inner–outer interactions in boundary layers (Baars *et al.* 2016; Cheng & Fu 2022*a*). In the present work, we will manipulate the 2-D SLSE to investigate the coupling between the velocity and the temperature fields, as well as the scale interactions in compressible channel flows. We will be dedicated to the related statistical characteristics of the temperature fluctuations and their consistency with the AEM, as they have not been thoroughly clarified as the velocity fluctuations in compressible wall-bounded turbulence.

The remainder of this paper is organized as follows. In § 2, the direct numerical simulation (DNS) data and the SLSE are described. In § 3, we present the general turbulence statistics and the flow structures associated with the $u$–$T$ coupling. The results of the linear-model-based study are provided for the near-wall, the logarithmic and the outer regions in § 4, separately, in the condition of $y_m = y_p$ and $y_m \neq y_p$. In § 5, some discussions are given, such as the Mach number effects on the results, and the relationship between the current results and the SRA. Concluding remarks are given in § 6.

## 2. The DNS database and linear model

### 2.1. *The DNS database*

In the present study, we carry out three simulations of supersonic channel flows at a bulk Mach number $M_b = U_b/C_w = 1.5$ ($U_b$ is the bulk velocity and $C_w$ is the speed of sound at wall temperature) and $Re_b = \rho_b U_b h/\mu_w = 3000$, 9400 and 20 020 ($\rho_b$ denotes the bulk density, $h$ the channel half-height and $\mu_w$ the dynamic viscosity at the wall). A series of DNSs at a bulk Mach number $M_b = 0.8$, and $Re_b = 3000$, $Re_b = 7667$ and $Re_b = 17\,000$ are also conducted. All these cases are performed in a computational domain of $4\pi h \times 2\pi h \times 2h$ in the streamwise ($x$), spanwise ($z$) and wall-normal ($y$) directions, respectively. Previous studies have verified that these set-ups of dimensions can capture most of the large-scale motions in the outer region of the boundary layer (Agostini & Leschziner 2014, 2019). Details of the parameter settings of the formed database are listed in table 1. The maximum number of grid points is in excess of one billion. The details of the DNS and validations of the cases Ma15Re9K, Ma15Re20K, Ma08Re8K and Ma08Re17K are provided by Cheng & Fu (2022*b*). A brief description of the computational set-ups and the data validations of the remaining cases are given in Appendix A.

Both the Reynolds- (denoted as $\bar{\phi}$) and the Favre-averaged (denoted as $\tilde{\phi} = \overline{\rho\phi}/\bar{\rho}$) statistics are used in the present study. The corresponding fluctuating components are represented as $\phi'$ and $\phi''$, respectively. Hereafter, we use the superscript $+$ to represent the normalization with $\rho_w$, the friction velocity (denoted as $u_\tau$, where $u_\tau = \sqrt{\tau_w/\rho_w}$, $\tau_w$ is the mean wall-shear stress), the friction temperature (denoted as $T_\tau$, where $T_\tau = Q_\mathrm{w}/\rho_w c_p u_\tau$, with $Q_\mathrm{w}$ and $c_p$ the mean heat flux on the wall and the specific heat at constant

| Case | $M_b$ | $Re_b$ | $Re_\tau$ | $Re_\tau^*$ | $\Delta x^+$ | $\Delta z^+$ | $\Delta y^+_{min}$ | $\Delta y^+_{max}$ | $Tu_\tau/h$ |
|---|---|---|---|---|---|---|---|---|---|
| Ma15Re3K | 1.5 | 3000 | 220 | 148 | 10.8 | 6.9 | 0.33 | 8.2 | 19.5 |
| Ma15Re9K | 1.5 | 9400 | 594 | 395 | 7.3 | 3.7 | 0.5 | 5.9 | 30.2 |
| Ma15Re20K | 1.5 | 20020 | 1150 | 780 | 9.3 | 4.7 | 0.49 | 6.9 | 13.1 |
| Ma08Re3K | 0.8 | 3000 | 192 | 168 | 8.9 | 4.5 | 0.43 | 4.5 | 39.5 |
| Ma08Re8K | 0.8 | 7667 | 436 | 382 | 10.8 | 6.9 | 0.44 | 5.4 | 15.3 |
| Ma08Re17K | 0.8 | 17000 | 882 | 778 | 10.8 | 6.5 | 0.63 | 6.4 | 20.4 |

Table 1. Parameter settings of the compressible DNS database. Here, $M_b$ denotes the bulk Mach number, and $Re_b$, $Re_\tau$ and $Re_\tau^*$ denote the bulk Reynolds number, friction Reynolds number and semi-local friction Reynolds number, respectively. Additionally, $\Delta x^+$ and $\Delta z^+$ denote the streamwise and spanwise grid resolutions in viscous units, respectively, $\Delta y^+_{min}$ and $\Delta y^+_{max}$ denote the finest and coarsest resolution in the wall-normal direction, respectively, and $Tu_\tau/h$ indicates the total eddy turnover time used to accumulate statistics.

pressure, respectively) and the viscous length scale (denoted as $\delta_\nu$, where $\delta_\nu = \nu_w/u_\tau$, with $\nu_w = \mu_w/\rho_w$). We also use the superscript $*$ to represent the normalization with the semi-local wall units, i.e. $u_\tau^* = \sqrt{\tau_w/\bar{\rho}}$ and $\delta_\nu^* = \overline{\nu(y)}/u_\tau^*$. Hence, the relationship between the semi-local friction Reynolds number and the friction Reynolds number is $Re_\tau^* = Re_\tau\sqrt{(\overline{\rho_c}/\bar{\rho}_w)}/(\overline{\mu_c}/\bar{\mu}_w)$. The subscript $c$ refers to the quantities evaluated at the channel centre. It is noted that the cases of Ma08Re3K, Ma08Re8K and Ma08Re17K share similar $Re_\tau^*$ with the cases of Ma15Re3K, Ma15Re9K and Ma15Re20K, respectively. In the present study, we mainly adopt the supersonic cases ($M_b = 1.5$) to investigate the $u$–$T$ coupling in compressible wall turbulence, whereas the subsonic cases ($M_b = 0.8$) primarily aid in elucidating the Mach number effects on the statistics in § 5.1. In addition, Gerolymos & Vallet (2014), Griffin, Fu & Moin (2021) and Bai, Griffin & Fu (2022) pointed out that the semi-local scalings, $Re_\tau^*$ and $y^*$, can reasonably clarify the Reynolds number effects on the statistics involving the thermodynamic and the velocity variables in compressible channel flows. Hence, we adopt them more frequently than $Re_\tau$ and $y^+$ in the present study.

### 2.2. *Linear model: spectral linear stochastic estimation*

The LSE (1.2) can be modified by conducting the estimation in the spectral domain (i.e. the spectral linear stochastic estimation), as the spectral characteristics of the signals can be preserved, and eliminates the contamination from the correlations between the orthogonal spectral modes (Tinney *et al.* 2006; Gupta *et al.* 2021). The DNS instantaneous fields at a given wall-normal height can be decomposed into Fourier coefficients along the streamwise and the spanwise directions by leveraging the homogeneity along these two directions. In the present study, we intend to study the physical characteristics of the temperature field associated with the velocity field in compressible wall turbulence; thus, SLSE is employed here and can be considered as a physics-based scale decomposition methodology for the temperature field. It takes the form of

$$T'_p(y_m, y_p) = F^{-1}_{x,z}\{H_T(\lambda_x, \lambda_z; y_m, y_p)F_{x,z}[u''_d(y_m)]\}, \tag{2.1}$$

where $u''_d$ denotes the density-weighted streamwise velocity fluctuation ($\sqrt{\rho}u''$) at $y_m$ (Patel *et al.* 2015). Very recently, Huang, Duan & Choudhari (2022) reported that the statistical characteristics of $\overline{\rho u''u''}/\tau_w$ in compressible boundary layers resemble those of $\overline{u'^2}^+$ in incompressible wall turbulence. This motives us to adopt $u''_d$ rather than $u''$ or $u'$

to represent the velocity streaks in compressible flows, in line with numerous previous studies (Patel *et al.* 2015; Sciacovelli, Cinnella & Gloerfelt 2017; Hirai, Pecnik & Kawai 2021; Huang *et al.* 2022) (we have verified that the results presented below are not changed even if $u''$ or $u'$ is employed). Here, $F_{x,z}$ and $F_{x,z}^{-1}$ denote the 2-D fast Fourier transform (2-D FFT) and the inverse 2-D FFT in the streamwise and the spanwise directions, respectively. Additionally, $H_T$ is the transfer kernel, which evaluates the correlation between $\hat{u}_d''(y_m)$ and $\hat{T}'(y_p)$ at streamwise length scale $\lambda_x$ and spanwise length scale $\lambda_z$, and can be calculated as

$$H_T(\lambda_x, \lambda_z; y_m, y_p) = \frac{\langle \hat{T}'(\lambda_x, \lambda_z; y_p)\breve{\hat{u}}_d''(\lambda_x, \lambda_z; y_m)\rangle}{\langle \hat{u}_d''(\lambda_x, \lambda_z; y_m)\breve{\hat{u}}_d''(\lambda_x, \lambda_z; y_m)\rangle}, \tag{2.2}$$

where $\langle\cdot\rangle$ represents the ensemble averaging, $\hat{T}'$ and $\hat{u}_d''$ are the Fourier coefficients of $T'$ and $u_d''$, respectively, and $\breve{\hat{u}}_d''$ is the complex conjugate of $\hat{u}_d''$. In this sense, $T_p'(y_m, y_p)$ in (2.1) is the component of $T'(y_p)$ that is linearly correlated with the $u_d''(y_m)$ at $y_m$, whereas $T_{np}' = T' - T_p'$ is the uncorrelated component (in fact, this treatment involves one hypothesis, i.e. there is no nonlinear scale interaction between $T_{np}'$ and $T_p'$. We will show that whether this assumption is true or not has no effect on the results exhibited below). To further gauge the coherence between $T'(y_p)$ and $u_d''(y_m)$, following Baars *et al.* (2016), a 2-D linear coherence spectrum (LCS) is also introduced here, and can be cast as

$$\gamma_c^2(\lambda_x, \lambda_z; y_m, y_p) = \frac{|\langle \hat{T}'(\lambda_x, \lambda_z; y_p)\breve{\hat{u}}_d''(\lambda_x, \lambda_z; y_m)\rangle|^2}{\langle|\hat{T}'(\lambda_x, \lambda_z; y_p)|^2\rangle\langle|\hat{u}_d''(\lambda_x, \lambda_z; y_m)|^2\rangle}, \tag{2.3}$$

where $|\cdot|$ is the modulus, and $\gamma_c^2$ evaluates the square of the scale-specific correlation between $T'(y_p)$ and $u_d''(y_m)$ with $0 \le \gamma_c^2 \le 1$ (Bendat & Piersol 2011). To be specific, $\gamma_c^2 = 1$ suggests a perfectly linear correlation between the velocity and the temperature signals at a wavelength pair $(\lambda_x, \lambda_z)$, whereas $\gamma_c^2 = 0$ implies a purely uncorrelated relationship.

According to Pirozzoli & Bernardini (2011), the temperature fluctuation in compressible wall turbulence can be envisioned as a wall-attached variable, similar to the streamwise velocity fluctuation. Thus, we employ two additional transfer kernels $H_L$, $H_w$, and one LCS to shed light on the wall coherence of $T_{np}'$ and $T_p'$. If $y_p$ is in the logarithmic or outer region, their footprints on the near-wall region can be predicted by

$$T_{\psi,L}'(y_p, y_i) = F_{x,z}^{-1}\{H_L(\lambda_x, \lambda_z; y_p, y_i)F_{x,z}[T_\psi'(y_p)]\}, \tag{2.4}$$

where $y_i$ is the wall-normal height of the near-wall position (set as $\Delta y_{min}$ listed in table 1) and $T_\psi'$ can be $T_{np}'$ or $T_p'$. The transfer kernel $H_L$ can be expressed by

$$H_L(\lambda_x, \lambda_z; y_p, y_i) = \frac{\langle \hat{T}'(\lambda_x, \lambda_z; y_i)\breve{\hat{T}}_\psi'(\lambda_x, \lambda_z; y_p)\rangle}{\langle \hat{T}_\psi'(\lambda_x, \lambda_z; y_p)\breve{\hat{T}}_\psi'(\lambda_x, \lambda_z; y_p)\rangle}. \tag{2.5}$$

The wall-coherent component of $T_\psi'$ can also be estimated by

$$T_{\psi,w}'(y_i, y_p) = F_{x,z}^{-1}\{H_w(\lambda_x, \lambda_z; y_i, y_p)F_{x,z}[T'(y_i)]\}, \tag{2.6}$$

with

$$H_w(\lambda_x, \lambda_z; y_i, y_p) = \frac{\langle \hat{T}_\psi'(\lambda_x, \lambda_z; y_p)\breve{\hat{T}}'(\lambda_x, \lambda_z; y_i)\rangle}{\langle \hat{T}'(\lambda_x, \lambda_z; y_i)\breve{\hat{T}}'(\lambda_x, \lambda_z; y_i)\rangle}. \tag{2.7}$$

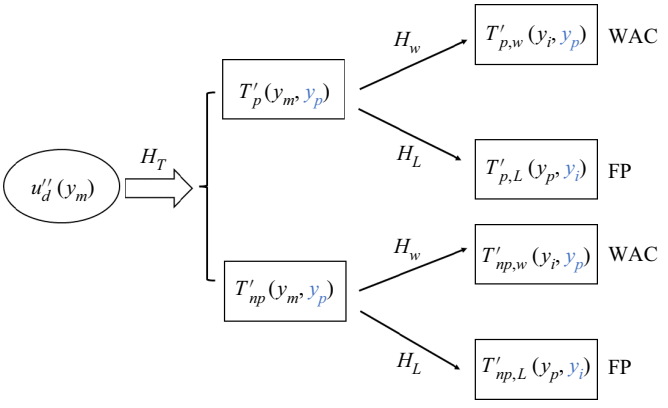


Figure 1. A sketch map of the linear-model-based study of the $u$–$T$ coupling and the temperature field in compressible wall turbulence. The abbreviations 'FP' and 'WAC' in the figure stand for footprint and wall-attached component, respectively. The wall-normal position in blue is the locus of the corresponding predicted variable.

Correspondingly, a wall-based LCS can also be defined as

$$\gamma_w^2(\lambda_x, \lambda_z; y_i, y_p) = \frac{|\langle \hat{T}'(\lambda_x, \lambda_z; y_i) \breve{\hat{T}}'_\psi(\lambda_x, \lambda_z; y_p) \rangle|^2}{\langle |\hat{T}'(\lambda_x, \lambda_z; y_i)|^2 \rangle \langle |\hat{T}'_\psi(\lambda_x, \lambda_z; y_p)|^2 \rangle}, \tag{2.8}$$

which manifests as a figure of merit for the wall coherence of $T'_\psi$.

Figure 1 is a sketch map of the linear-model-based study of the $u$–$T$ coupling in compressible wall turbulence. To sum up, three wall-normal positions involved in the present study are:

(1) $y_m$ – the wall-normal locus of the measured density-weighted streamwise velocity fluctuation;
(2) $y_p$ – the wall-normal locus of the predicted temperature fluctuation;
(3) $y_i$ – a near-wall location, and is set as $\Delta y_{min}$ listed in table 1 for each case.

The physical variables involved in the present study are:

(1) $u''_d(y_m)$ – the density-weighted streamwise velocity fluctuation ($\sqrt{\rho}u''$) at $y_m$;
(2) $T'(y_p)$ – the temperature fluctuation at $y_p$;
(3) $T'(y_i)$ – the temperature fluctuation at a near-wall position $y_i$;
(4) $T'_p(y_m, y_p)$ – the component of $T'(y_p)$ that is linearly correlated with $u''_d(y_m)$, which is calculated by an $H_T$-based estimation according to (2.1) and (2.2);
(5) $T'_{np}(y_p)$ – the component of $T'(y_p)$ that is not linearly correlated with $u''_d(y_m)$, namely $T'_{np}(y_p) = T'(y_p) - T'_p(y_m, y_p)$;
(6) $T'_{\psi,L}(y_p, y_i)$ – the footprint of $T'_\psi$ on the near-wall location $y_i$ ($y_i = \Delta y_{min}$), which is calculated by an $H_L$−based estimation according to (2.4) and (2.5), where $T'_\psi$ can be $T'_p$ or $T'_{np}$;
(7) $T'_{\psi,w}(y_i, y_p)$ – the wall-attached component of $T'_\psi$, which is calculated by an $H_w$−based estimation according to (2.6) and (2.7).

Moreover, the three transfer kernels involved in the present study are:

(1) $H_T$ – it gauges the correlation between $\hat{u}''_d(y_m)$ and $\hat{T}'(y_p)$ at length scales $\lambda_x$ and $\lambda_z$;
(2) $H_L$ – it gauges the correlation between $\hat{T}'_\psi(y_p)$ and $\hat{T}'(y_i)$ at length scales $\lambda_x$ and $\lambda_z$ for the estimation of $T'_{\psi,L}(y_p, y_i)$;
(3) $H_w$ – it gauges the correlation between $\hat{T}'_\psi(y_p)$ and $\hat{T}'(y_i)$ at length scales $\lambda_x$ and $\lambda_z$ for the estimation of $T'_{\psi,w}(y_i, y_p)$;

The two LCSs involved in the present study are:

(1) $\gamma_c^2$ – it evaluates the square of the scale-specific correlation between $T'(y_p)$ and $u''_d(y_m)$ with $0 \leq \gamma_c^2 \leq 1$;
(2) $\gamma_w^2$ – it evaluates the square of the scale-specific correlation between $T'(y_i)$ and $T'_\psi(y_p)$ with $0 \leq \gamma_w^2 \leq 1$.

The proposed framework here aids in studying the statistical characteristics of the temperature fluctuation, particularly its coherence with the streamwise velocity fluctuation, and the consequent scale interactions with the near-wall turbulence. Similar numerical frameworks have been adopted by the authors to investigate the attached eddies in incompressible channel flows in previous studies (Cheng & Fu 2022*a*; Cheng *et al.* 2022; Cheng & Fu 2023). It bears emphasizing that the two fields are also entwined with each other along the time dimension. Hence, the temporal frequency can also be invoked in the SLSE presented above, which can further provide the frequency structure of the multi-physics coupling (Tinney *et al.* 2006). However, a reliable temporal analysis demands a large number of time-resolved DNS samples, which is far beyond our capacity. Accordingly, we only conduct spatial analyses and do not consider the frequency characteristics of the coupling at the present stage.

## 3. General turbulence statistics and flow structures

We start by providing an overview of the general turbulence statistics and flow structures related to the temperature field and the $u$–$T$ coupling in supersonic cases. Figure 2(*a*) displays the variations of the temperature fluctuation intensities as functions of the wall-normal height $y/h$ for all the supersonic cases. The peak of $\overline{T'^2}^+$ grows in magnitude as the Reynolds number increases and its wall-normal location moves closer to the wall concurrently. If the profiles are plotted with the abscissa in semi-local coordinates $y^*$, the maxima of $\overline{T'^2}^+$ in various cases are roughly positioned at an identical wall-normal position $y^* \approx 10$, as shown in figure 2(*b*). Similar behaviours have been reported for the streamwise velocity fluctuation in incompressible (Marusic, Baars & Hutchins 2017; Smits *et al.* 2021) and compressible (Modesti & Pirozzoli 2016; Yao & Hussain 2020) wall turbulence. This scenario indicates the similarity between the momentum and the heat transfer in the vicinity of the wall. The magnitude increase of the normalized fluctuation intensity of a wall-attached variable in the near-wall region is typically attributed to the amplification of the inner–outer interactions as the Reynolds number rises (Marusic *et al.* 2017; Cheng *et al.* 2020*a*; Smits *et al.* 2021). If this is true, it hints at the fact that the temperature fluctuation in compressible flow can also be treated as an attached variable. This claim will be verified in §§ 4 and 5.1.

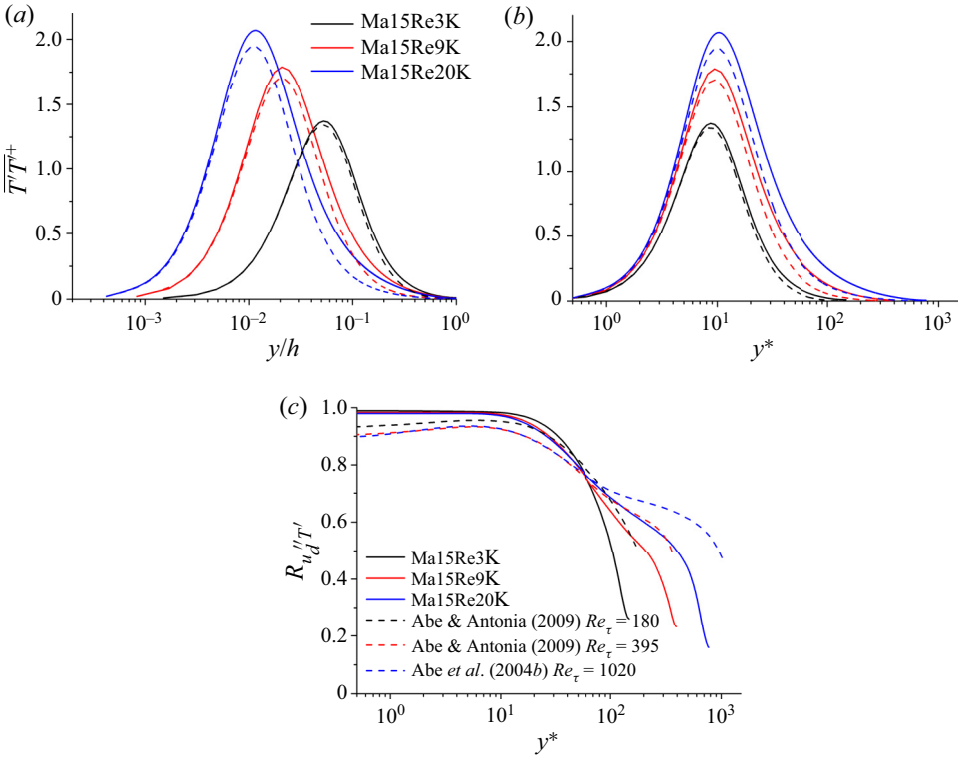


Figure 2. (*a*,*b*) Variations of $\overline{T'^2}^+$ (solid lines) and $\overline{T_p'^2}^+$ ($y_m = y_p$) (dashed lines) as functions of the wall-normal height (*a*) $y/h$ and (*b*) $y^*$ for all the supersonic cases; (*c*) correlation coefficients $R_{u_d''T'}$ as functions of $y^*$ for all the supersonic cases, and the counterparts from incompressible channel flows at similar $Re_\tau$ (Abe *et al.* 2004*b*; Abe & Antonia 2009) are exhibited by dashed lines for comparison.

Figure 2(*c*) shows the variations of the correlation coefficients between $T'$ and $u_d''$ for all the supersonic cases. The definition of the correlation coefficient takes the form of

$$R_{u_d''T'} = \frac{\langle u_d''T' \rangle}{u_{d,rms}''T'_{rms}}, \tag{3.1}$$

where the subscript '*rms*' denotes the root mean square of the corresponding variable. It can be observed that regardless of the Reynolds number magnitude, there is a positive correlation between $T'$ and $u_d''$ throughout the whole channel. The magnitude of $R_{u_d''T'}$ is approximately equal to unity in the range of $y^* < 10$, and decreases monotonously as $y^*$ increases. In the logarithmic region, the decreasing trend of $R_{u_d''T'}$ is gradual; nevertheless, it accelerates in the outer region, particularly for the case Ma15Re20K. These results are consistent with some previous studies of turbulent channel flows at disparate Mach numbers and Reynolds numbers (Huang *et al.* 1995; Foysi, Sarkar & Friedrich 2004; Brun *et al.* 2008). The correlations between these two fields at similar $Re_\tau$ are slightly higher for the compressible flows than those of the incompressible flows in the near-wall region, and lower in the outer region (see dashed lines in figure 2*c*). It may indicate that the compressibility enhances the similarity between the two fields in the vicinity of the wall, and diminishes it in the outer region.

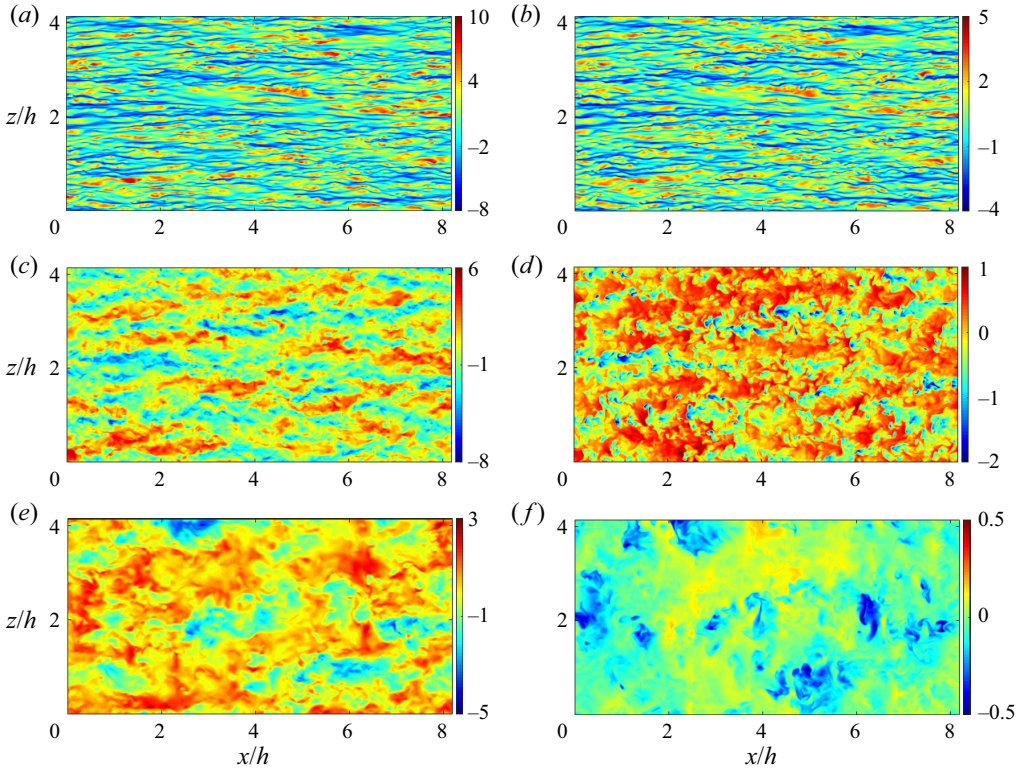


Figure 3. (*a*,*c*,*e*) Top view of the instantaneous density-weighted streamwise velocity fluctuation field $u_d''^+$ at (*a*) $y^* \approx 10$, (*c*) $y \approx 0.15h$ and (*e*) $y \approx 0.85h$ for the case Ma15Re20K; (*b*,*d*,*f*) top view of the instantaneous temperature fluctuation field $T'^+$ at (*b*) $y^* \approx 10$, (*d*) $y \approx 0.15h$ and (*f*) $y \approx 0.85h$ for the case Ma15Re20K.

To characterize vividly the relationship between the velocity and the temperature structures, figure 3 shows the top view of the instantaneous $u_d''^+$ and $T'^+$ fields of the case Ma15Re20K at three selected wall-normal positions. Other cases share similar characteristics and are not shown here for brevity. For the near-wall position $y^* \approx 10$, where $R_{u_d''T'} \approx 1$, the velocity and temperature streaks share virtually identical morphological characteristics and the occurrences of the corresponding extreme events are roughly synchronous. For the logarithmic region $y \approx 0.15h$ with $R_{u_d''T'} \approx 0.67$, the length scales of the velocity streaks become larger, whereas the temperature fluctuations display the mushroom shapes and are more isotropic than their near-wall counterparts. However, it is still effortless to observe the strong links between the low-speed velocity streaks and the negative temperature fluctuations. When the observation wall-normal position is moved to the channel centre $y \approx 0.85h$ with $R_{u_d''T'} \approx 0.26$, in contrast to the velocity fluctuations shown in figure 3(*e*), the temperature fluctuations are characterized by spotted extreme events without discernible streaky shapes. The shapes of $T'$ structures are more isotropic. It underscores the fact that the coupling between the two fields is rather weak in the outer region. The above inspections, which are conducted at various wall-normal planes, are consistent with the variation tendency of $R_{u_d''T'}$ as seen in figure 2(*c*). It is interesting to note that Pirozzoli & Bernardini (2011) also reported comparable findings on the temperature streaks for a supersonic boundary layer with adiabatic wall condition at a similar $Re_\tau$.

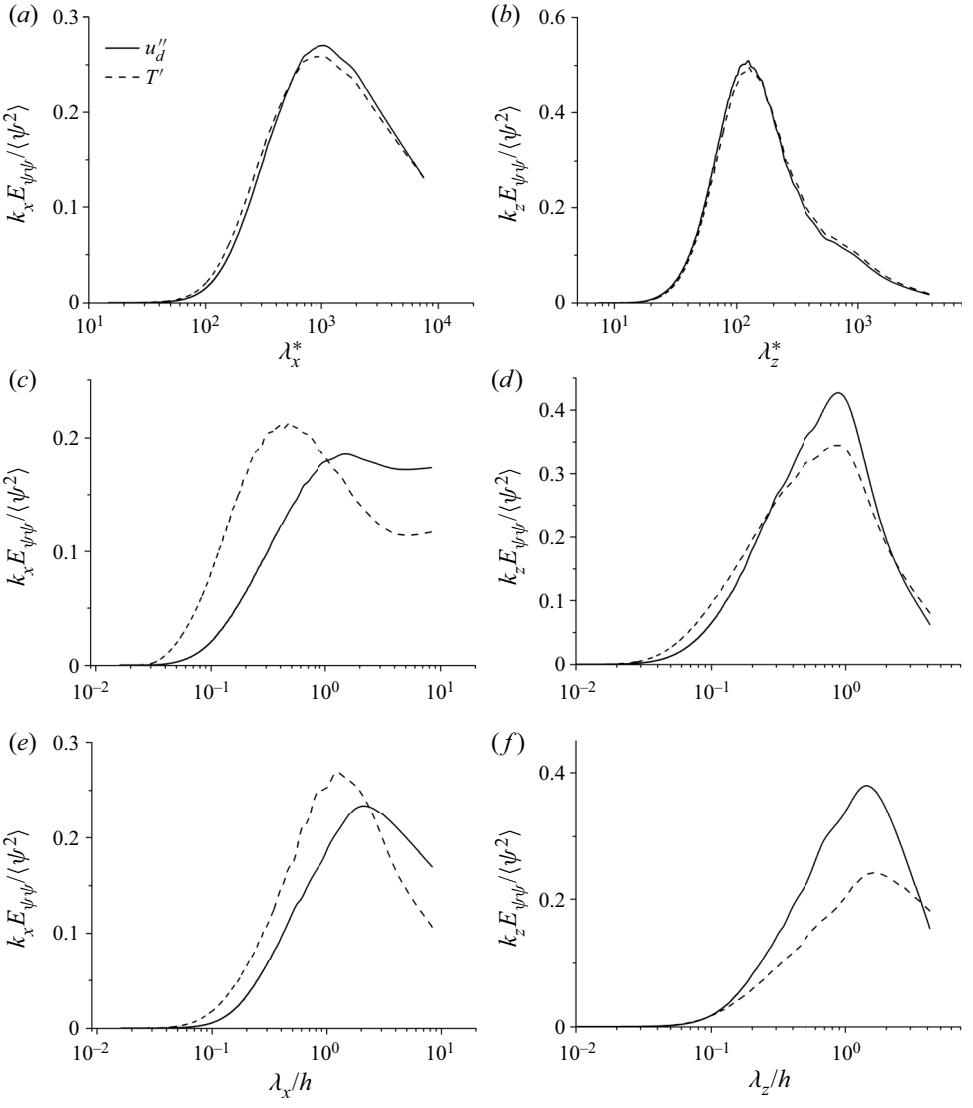


Figure 4. (*a*,*c*,*e*) Premultiplied streamwise spectra of $u_d''$ and $T'$ at (*a*) $y^* \approx 10$, (*c*) $y \approx 0.15h$ and (*e*) $y \approx 0.85h$ for the case Ma15Re20K; (*b*,*d*,*f*) premultiplied spanwise spectra of $u_d''$ and $T'$ at (*b*) $y^* \approx 10$, (*d*) $y \approx 0.15h$ and (*f*) $y \approx 0.85h$ for the case Ma15Re20K. These spectra are normalized by the energy of $\psi$ at a given wall-normal height.

Finally, it is instructive to compare the premultiplied spectra of $u_d''$ and $T'$ at different wall-normal positions (denoted as $kE_{\psi\psi}$, where $\psi$ can be $u_d''$ or $T'$), which are exhibited in figure 4. The specific spectral peak at a given wall-normal position may not be identical for each case, considering their distinct Reynolds numbers. We only show the results of the case Ma15Re20K here due to its relatively sufficient scale separation. To facilitate comparison, these spectra are normalized by the energy of $\psi$ at a given wall-normal height. The premultiplied spectra of $u_d''$ and $T'$, whether the streamwise or the spanwise spectra, almost overlap with one another in the buffer layer. Moreover, their peaks are located at $\lambda_x^* \approx 1000$ and $\lambda_z^* \approx 100$, which are consistent with the well-documented spectral scale

characteristics of the near-wall turbulence in incompressible flow (Kline *et al.* 1967; Kim, Moin & Moser 1987; Hwang 2013). When the observation wall-normal location is moved to the logarithmic layer, their disparities start to stand out. It can be seen that the typical streamwise length scales of velocity streaks are longer than those of the temperature, but their spanwise length scales are nearly identical, i.e. $\lambda_z \approx 0.8h$, just like those in incompressible flows (Ahn *et al.* 2015; Abe, Antonia & Toh 2018). In the outer region, the peaks of their streamwise spectra are still divergent, that is, $\lambda_x \approx 2h$ and $\lambda_x \approx 1h$ for $u_d''$ and $T'$, respectively. However, their spectral peaks of the spanwise spectra share equivalent length scale $\lambda_z \approx 1.4h$. Hence, the shapes of the temperature streaks are more isotropic than those of velocity streaks in the outer region. Overall, the spanwise length scales of $T'$ are in line with those of $u_d''$ spanning the whole channel. As the attached eddies are self-similar with their spanwise length scales (Lozano-Durán *et al.* 2012; Hwang 2015; Cheng *et al.* 2019), it underlines the fact again that the temperature fluctuation in compressible flow can also be treated as an attached variable. It also signifies that the $H_w$, a wall-based kernel function introduced in § 2.2, is of physical significance. In the next section, we elaborate on dissecting the coupling between $u_d''$ and $T'$ within the linear-model framework built in § 2.2. Furthermore, the statistical characteristics of $T'$ will also be investigated through the prism of the AEM.

## 4. Results of linear-model-based analysis

The linear-model-based analysis includes two branches, i.e. $y_m = y_p$ and $y_m \neq y_p$ for (2.1) to (2.3). The former represents that the wall-normal position of the inputted $u_d''$ is the same as that of $T'$, whereas the latter is the opposite. The results of them will be reported in turn.

### 4.1. *Linear-model-based analysis with* $y_m = y_p$

#### 4.1.1. *Overall picture*

Before proceeding with the detailed analysis, it is better to have a rough idea of the effectiveness of the linear coupling model. The dashed lines in figure 2(*a*,*b*) show the magnitudes of $\overline{T_p'^2}^+$ as functions of $y_p/h$ and $y_p^*$ for all the supersonic cases, respectively. Here, $T_p'$ is calculated by an $H_T-$based estimation according to (2.1) and (2.2). It can be seen that only below the buffer layer can the temperature fluctuation intensities be largely captured by the linear model. This observation can be further verified by inspecting the relative deviations (RDs) displayed in figure 5. The definition of RD takes the form of

$$\mathrm{RD} = \frac{\overline{T'^2}^+ - \overline{T_p'^2}^+}{\overline{T'^2}^+}. \tag{4.1}$$

The linear model can recover over 95 % of $\overline{T'^2}^+$ for $y_p^* < 10$. This relative error, however, rapidly increases as the wall-normal height increases. Taking the case Ma15Re20K as an example, only 50 % fluctuation intensity of $T'$ can be adequately captured at $y_p^* \approx 100$. An interesting thing worthy of note is that, for the case with the highest Reynolds number, there is a wall-normal position in the outer region, $y_p \approx 0.5h$, where RD begins to increase more rapidly than in the logarithmic region. This indicates that the effectiveness of the linear coupling model degenerates more severely as $y_p$ approaches the channel centre. The overall variation tendency is consistent with the correlations shown in figure 2(*c*), and it is reminiscent of the variation of the similarity between the velocity and temperature

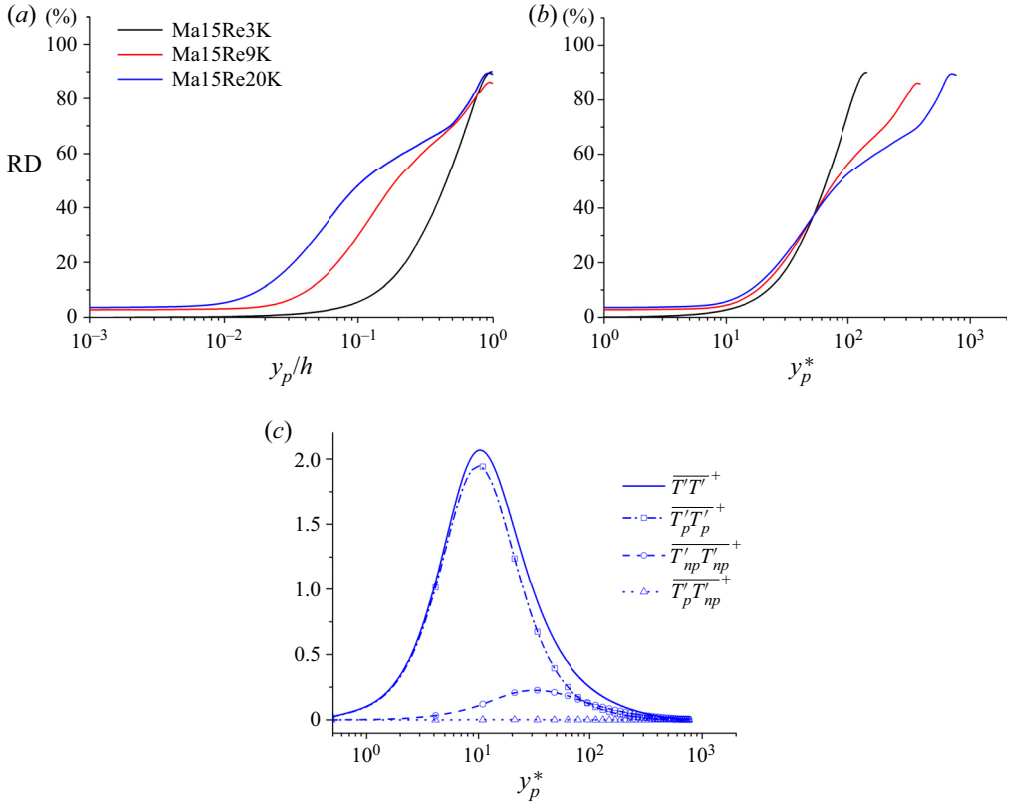


Figure 5. (*a*,*b*) Relative deviations (RDs) as functions of (*a*) $y_p/h$ and (*b*) $y_p^*$ for all the supersonic cases. Here, $y_p$ is equal to $y_m$ for these cases under consideration; (*c*) variations of $\overline{T'^2}^+$, $\overline{T'^2_p}^+$, $\overline{T'^2_{np}}^+$ and $\overline{T'_pT'_{np}}^+$ as functions of the wall-normal height $y_p^*$ for the case Ma15Re20K.

fluctuations in incompressible flow at the molecular Prandtl number $Pr$ close to unity. That is, there is a strong similarity in the near-wall region, while it is weakened away from the wall (Abe & Antonia 2009; Antonia *et al.* 2009; Pirozzoli, Bernardini & Orlandi 2016). However, based on the linear model, the temperature fluctuation intensity $\overline{T'^2}^+$ can be decomposed as

$$\overline{T'^2}^+ = \overline{T'^2_p}^+ + \overline{T'^2_{np}}^+ + 2\overline{T'_pT'_{np}}^+. \tag{4.2}$$

Figure 5(*c*) shows the variations of $\overline{T'^2}^+$, $\overline{T'^2_p}^+$, $\overline{T'^2_{np}}^+$ and $\overline{T'_pT'_{np}}^+$ as functions of the wall-normal height $y_p^*$ for the case Ma15Re20K. As seen, the magnitudes of $\overline{T'^2_p}^+$, $\overline{T'^2_{np}}^+$ are non-negligible, whereas $\overline{T'_pT'_{np}}^+$ nearly equals zero. It indicates that the interaction between $T'_p$ and $T'_{np}$ have no contribution to the even-order moments of $T'$. Other cases show similar results. We will ignore this interaction term in the following study.

Accordingly, the entire channel can be divided into three regions for the purpose of the linear-model-based analysis: (1) the near-wall region, where RD $\approx$ 5 %; (2) the logarithmic region and the lower part of the outer region; and (3) the outer region in the vicinity of the channel centre, where the effectiveness of the linear coupling model

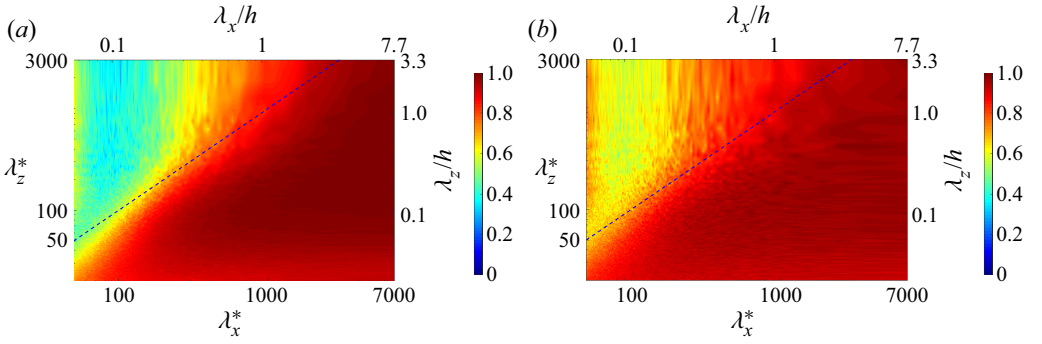


Figure 6. (*a*) The $\gamma_c^2$ spectrum for the case Ma15Re20K when $y_m^* = y_p^* \approx 10$; (*b*) $R_{pm}$ spectrum for the case Ma15Re20K when $y_m^* = y_p^* \approx 10$. The dashed lines in panels (*a*,*b*) denote $\lambda_x^* = \lambda_z^*$.

is the worst. We will dissect these three regions separately and shed light on the linear coupling relationship between $u_d''$ and $T'$ in the following subsections.

#### 4.1.2. *Near-wall region ($y_m^* = y_p^* \approx 10$)*

We recall from (2.3) that $\gamma_c^2$ is a measure of coherence between $T'(y_p)$ and $u_d''(y_m)$ ($\gamma_c^2 = 1$ indicates a prefect coherence and $\gamma_c^2 = 0$ indicates no coherence). Figure 6(*a*) shows the $\gamma_c^2$ spectrum when $y_m^* = y_p^* \approx 10$ for the case Ma15Re20K. It is interesting to note that the temperature streaks are perfectly coherent with the velocity streaks at the typical near-wall turbulence length scales ($\lambda_x^* \approx 1000$ and $\lambda_z^* \approx 100$, see figure 4*a*,*b*). It shows that the streamwise velocity fluctuations and temperature fluctuations carried by the near-wall motions are entirely coherent. This is the reason why $R_{u_d''T'} \approx 1$ in the buffer layer (see figure 2*c*). Moreover, we note that for the large-scale temperature fluctuations ($\lambda_x > 1h$ and $\lambda_z > 0.5h$), the magnitudes of $\gamma_c^2$ also approach unity. It implies that the footprints of large-scale $T'$ and $u_d''$ in the near-wall region are also well coherent. In contrast, only the small-scale and 'fat' motions ($\lambda_z^* > \lambda_x^*$) lose the perfect coherence. Other cases bear similar results and are not shown here for brevity.

Another way to gauge the linear coupling between these two signals is to investigate the relative magnitude $R_{pm}$ associated with $\hat{T}_p'$ and $\hat{T}'$ at different length scales (Gupta *et al.* 2021), namely,

$$R_{pm}(\lambda_x, \lambda_z; y_m, y_p) = \sqrt{\langle|\hat{T}_p'(\lambda_x, \lambda_z; y_m, y_p)|^2\rangle / \langle|\hat{T}'(\lambda_x, \lambda_z; y_p)|^2\rangle}, \tag{4.3}$$

which are shown in figure 6(*b*) for the case M15Re20K. It appears that the energy of the streamwise elongated structures ($\lambda_x^* > \lambda_z^*$) can be almost completely recovered by the linear model, whereas for those of the 'fat' motions ($\lambda_z^* > \lambda_x^*$), the present approach loses some capabilities. This scenario is consistent with the $\gamma_c^2$ spectrum shown in figure 6(*a*). We have checked that almost all the morphological properties of the instantaneous $T'^+$ displayed in figure 3(*b*) are recovered by $T_p'^+$ (not shown here). This is because the majority of the energetic motions populating the buffer layer are captured by the linear model.

At the end of this subsection, it is instructive to compare the probability density functions (p.d.f.s) of $T_p'^+$ and $T'^+$ to distinguish whether some extreme events of $T'^+$ are predictable for the linear model. They are plotted in figure 7(*a–c*). For the positive extreme events ($T'^+ > 0$), the linear model overestimates their probabilities of occurrence, whereas

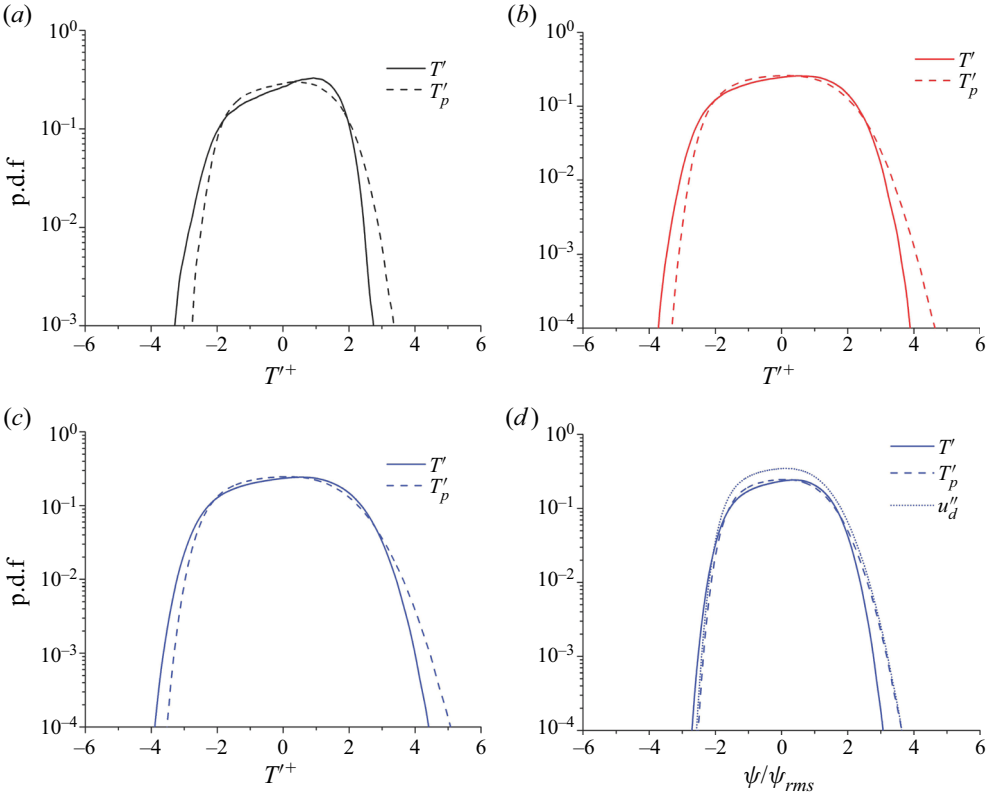


Figure 7. (*a*,*b*,*c*) The p.d.f.s of $T_p'^+(y_p^* = y_m^* \approx 10)$ and $T'^+(y^* \approx 10)$ for the case (*a*) Ma15Re3K, (*b*) Ma15Re9K and (*c*) Ma15Re20K. (*d*) The p.d.f.s of $T_p'(y_p^* = y_m^* \approx 10)$, $T'(y^* \approx 10)$ and $u_d''(y^* \approx 10)$ for the case Ma15Re20K. Each variable is normalized by its root mean square (r.m.s.) value in panel (*d*). The $\psi$ in the abscissa of panel (*d*) stands for the corresponding variable.

for the negative extreme events ($T'^+ < 0$), the contrary is the case. The Reynolds number has no bearing on the conclusion. In other words, even while the linear coupling model can recapture the fundamental properties of the temperature field in the buffer layer, it is not able to reliably identify the extreme thermal events. Figure 7(*d*) shows the p.d.f.s of $T_p'(y_p^* = y_m^* \approx 10)$, $T'(y^* \approx 10)$ and $u_d''(y^* \approx 10)$ for the case Ma15Re20K. To facilitate comparison, each variable is normalized by its r.m.s. value. Other cases show similar results and are not shown here. A noteworthy observation is that the p.d.f. of $T_p'$ bears similar shape with that of $u_d''$ rather than $T'$. This is the limitation of the linear model, i.e. the instantaneous distribution of the predicted variable is controlled by that of the measured variable (the results of other wall-normal positions also obey this criterion, see figures 11*c* and 18*b*). Only with quadratic estimation techniques and above can the p.d.f. of the predicted variable be modified and closer to the actual flow (Tinney *et al.* 2006).

4.1.3. *Logarithmic region ($y_m = y_p \approx 0.1h$–$0.2h$)*

For the logarithmic region, the effectiveness of the linear model is not as excellent as it is in the buffer layer. Taking the case Ma15Re20K as an example, at $y_m = y_p \approx 0.15h$, the

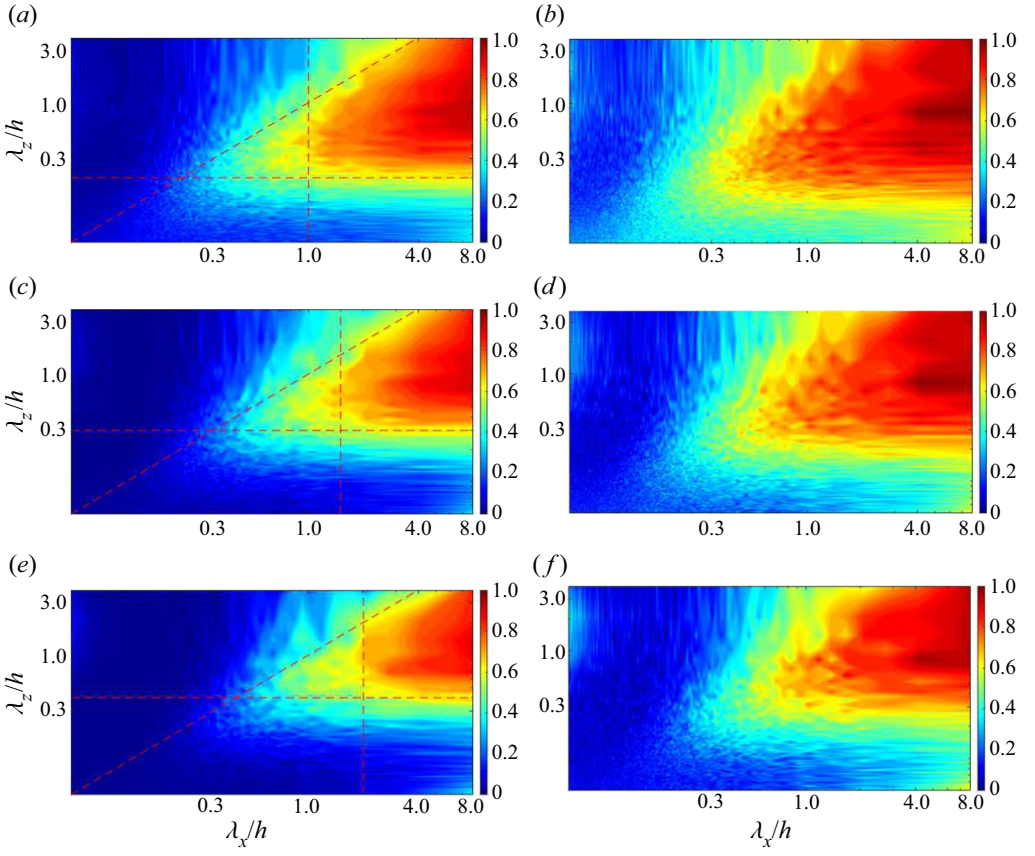


Figure 8. (*a*,*c*,*e*) The $\gamma_c^2$ spectra for the case Ma15Re20K when (*a*) $y_m = y_p \approx 0.1h$, (*c*) $y_m = y_p \approx 0.15h$, (*e*) $y_m = y_p \approx 0.2h$; (*b*,*d*,*f*) $R_{pm}$ spectra for the case Ma15Re20K when (*b*) $y_m = y_p \approx 0.1h$, (*d*) $y_m = y_p \approx 0.15h$, (*f*) $y_m = y_p \approx 0.2h$. The dashed oblique lines in panels (*a*,*c*,*e*) denote $\lambda_x = \lambda_z$, and the dashed transverse and the vertical lines denote $\lambda_z = 2y_p$ and $\lambda_x = 10y_p$, respectively.

RD is 55 %. A non-negligible fraction of fluctuation intensity cannot be captured by the linear model.

The $\gamma_c^2$ spectra of the case Ma15Re20K for $y_m = y_p \approx 0.1h$, $0.15h$ and $0.2h$ are shown in figures 8(*a*), 8(*c*) and 8(*e*), respectively. It is noted that we only report the results of case Ma15Re20K in this subsection due to its relatively wider spanning of the logarithmic region. It is not difficult to observe that only the streamwise elongated fluctuations ($\lambda_x > \lambda_z$) of $T'$ and $u_d''$ are highly coupled. This scenario is identical to that of the buffer layer (see figure 6). Additionally, there is only a small portion of the scale range where the magnitude of $\gamma_c^2$ is remarkable. By dissecting the $\gamma_c^2$ spectra of the disparate wall-normal positions in the logarithmic region displayed in figure 8, this range can be roughly bounded by

$$\lambda_x > \lambda_z, \quad \lambda_x > 10y_p, \quad \lambda_z > 2y_p. \tag{4.4a–c}$$

Figure 8(*b*,*d*,*f*) show the $R_{pm}$ spectra at the corresponding three wall-normal locations, respectively. It is transparent that the energy in the range defined by (4.4*a–c*) can be predominantly recovered by the linear model. The scale-based linear coupling can also be recognized by comparing the instantaneous $T'^{+}$ and $T_p'^{+}$ at $y = 0.15h$, which are illustrated in figure 9(*a*). As seen, only the long streaks of $T'^{+}$ are maintained in the

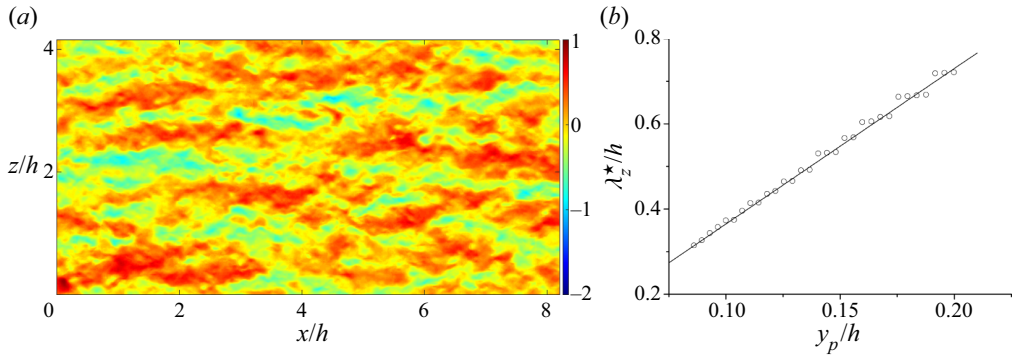


Figure 9. (*a*) Top view of the instantaneous $T_p^{'+}$ field when $y_m = y_p \approx 0.15h$ for the case Ma15Re20K. (*b*) Variation of $\lambda_z^\star/h$ as a function of $y_p/h$ in the logarithmic region for Ma15Re20K. In panel (*b*), the DNS results are presented by circles and the black line denotes $\lambda_z^\star = 3.6y_p$.

instantaneous $T_p^{'+}$. Additionally, $T_p^{'+}$ resembles the filtered $u_d^{''+}$ (see figure 3*c*), and $T_p^{'+}$ and $T^{'+}$ (see figure 3*d*) seem to organize similarly along the spanwise direction rather than the streamwise direction. These observations are similar to the finite similarities between the velocity and scalar fields reported in incompressible wall turbulence (Antonia *et al.* 2009).

Moreover, some details also deserve attention. First, the peaks of $\gamma_c^2$ are located at $\lambda_z \approx 1h$–$1.5h$ for the three selected wall-normal positions, which is the spanwise spacing of the very-large-scale motions (VLSMs) in the outer region of the incompressible and supersonic turbulent boundary layers (Del Álamo & Jiménez 2003; Abe *et al.* 2004*a*; Ganapathisubramani, Clemens & Dolling 2006; Hutchins & Marusic 2007). It signifies that VLSMs can not only permeate into the near-wall and the logarithmic regions, but also be actively linked with the temperature streaks in the compressible wall turbulence. Second, it is intriguing that the range boundaries defined by (4.4*a–c*) follow the scales of the self-similar wall-attached motions in wall turbulence. To name but a few, Deshpande, Monty & Marusic (2021) analysed the scale characteristics of the active motions (i.e. the self-similar attached eddies) in the logarithmic region of the boundary layers, and found their geometric shapes obey $\lambda_x \approx 10y$ and $\lambda_z \approx 3y$. Hwang, Lee & Sung (2020) also pointed out that the lower bound of the linear behaviours of the self-similar wall-attached structures in wall turbulence follows $\lambda_x > 12y$ and $\lambda_x = 4\lambda_z$. These pioneer results are all very close to the scale-range estimation provided by (4.4*a–c*). Hence, it is sensible to envision that the temperature streaks coupling the velocity field in the compressible flow are considerably wall-attached. They consist of two components, e.g. one is the self-similar wall-attached motions described by the AEM (Townsend 1976; Perry & Chong 1982); the other is VLSMs which can also exert significant influences on the near-wall flow (Perry & Marusic 1995; Cheng *et al.* 2019; Yoon *et al.* 2020).

To further characterize the energetic scales in LCS of the logarithmic region, we define the $\gamma_c^2$−weighted average spanwise wavenumber $k_z^\star(y)$ and the corresponding length scale $\lambda_z^\star = 2\pi/k_z^\star(y)$. The definition of $k_z^\star$ takes the form of

$$k_z^\star(y) = \frac{\int_\Omega k_z \gamma_c^2(y; k_x, k_z)\,\mathrm{d}k_x\,\mathrm{d}k_z}{\int_\Omega \gamma_c^2(y; k_x, k_z)\,\mathrm{d}k_x\,\mathrm{d}k_z}, \tag{4.5}$$

where $\Omega$ is the spectral domain defined by (4.4*a–c*), i.e. the energetic scale range of the LCS in the logarithmic region. It is the spanwise length scale rather than the streamwise one that is taken into account here, as previous studies provide compelling evidence that the energy-containing motions in the logarithmic region are self-similar with their spanwise length scales (Del Álamo *et al.* 2004; Hwang 2015; Cheng *et al.* 2019). Figure 9(*b*) shows the variation of $\lambda_z^\star/h$ as a function of $y_p/h$ in the logarithmic region for Ma15Re20K. It can be seen that there is a linear relationship between $\lambda_z^\star/h$ and $y_p/h$. This observation underscores the fact that the temperature and velocity fields are linearly coupled within the self-similar scale range. The variation of $\gamma_c^2$ spectra along the wall-normal direction in the logarithmic region is chiefly ascribed to the self-similar eddies.

The above argument can also be validated by inspecting the $\gamma_w^2$ spectra of $T_p'^+$ and $T_{np}'^+$ as per (2.8), which evaluate the wall coherence of these two signals. Herein, $T_{np}' = T' - T_p'$ is the uncoupling component of $T'$. The results are displayed in figure 10 for the three corresponding wall-normal planes in the logarithmic region. Only the motions of $T_p'$ within the scale range roughly given by (4.4*a–c*) are coherent with the near-wall flow, whereas for $T_{np}'$, no coherence can be observed. This observation supports our claim above. Nearly all the wall-attached temperature streaks are contained in $T_p'$, rather than $T_{np}'$. It is noted that the $\gamma_w^2$ spectra given here (figure 10*a*,*c*,*e*) and the $\gamma_c^2$ spectra shown in figures 8(*a*), 8(*c*) and 8(*e*) are not identical. It suggests that some $T'$ motions coupled with $u_d''$ are wall-detached in the logarithmic region indeed.

Figure 11(*a*) shows the variations of the fluctuation intensities of $T'$, $T_p'$, $T_{p,w}'$ and $T_{np,w}'$ as functions of the wall-normal height $y/h$ in the logarithmic region. Herein, $T_{p,w}'$ and $T_{np,w}'$ are the wall-attached components of $T_p'$ and $T_{np}'$, respectively, which can be estimated by an $H_w$-based estimation according to (2.6) and (2.7). As can be seen, the intensity of $T_{p,w}'$ occupies approximately 34 % of $\overline{T_p'^2}^+$ in the logarithmic region (equivalent to 15 % of $\overline{T'^2}^+$), whereas the magnitude of $T_{np,w}'$ is negligible. It shows once again that almost all the temperature streaks that are attached to the wall are contained in $T_p'$ rather than $T_{np}'$. Figure 11(*b*) compares the p.d.f.s of the instantaneous $T'$, $T_p'^+$ and $T_{p,w}'^+$ at $y/h = 0.1$. The p.d.f. of $T_{p,w}'^+$ is found to be more symmetric than those of the other two signals with invisible extreme events. This phenomenon hints that the small-scale $T'$ motions, which cannot be captured by the linear model, are more intermittent than the large-scale counterparts. Figure 11(*c*) displays the p.d.f.s of $T'$, $T_p'$ and $u_d''$ at $y/h = 0.1$. All variables are normalized by their r.m.s. values. As expected, the p.d.f. of $T_p'$ has a similar shape with that of $u_d''$.

Since it is demonstrated that the wall-attached component of $T'$ is contained in $T_p'$, it is instructive to inspect its statistical characteristics and compare with the celebrated attached-eddy hypothesis (Townsend 1976; Perry & Chong 1982). In our previous work (Cheng & Fu 2022*a*), we have proposed an operable framework to reach this goal. To be specific, for a wall-attached variable $\phi$ in the logarithmic region between $y_s^*$ and $y_p^*$ ($y_s^*$ denotes the lower bound of the logarithmic region and is set as 80 in the present study), if its representative spatial structures are arranged in a hierarchical manner which can be adequately depicted by the AEM, the momentum generation function of its footprint in the near-wall region ($\phi_L$) should follow a so-called strong self-similarity (SSS), i.e.

$$\langle \exp(q\phi_L) \rangle \sim \left( \frac{y_p}{y_s} \right)^{s(q)}, \tag{4.6}$$

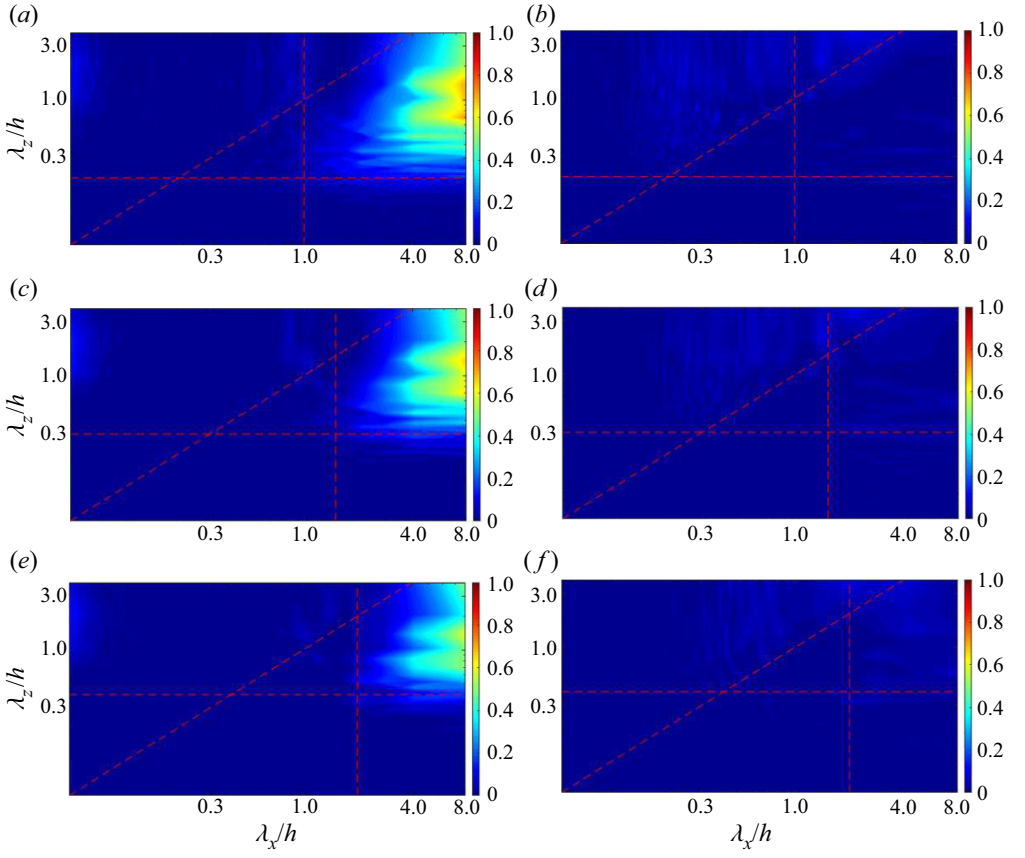


Figure 10. (*a*,*c*,*e*) The $\gamma_w^2$ spectra of $T_p^{'+}$ for the case Ma15Re20K when (*a*) $y_m = y_p \approx 0.1h$, (*c*) $y_m = y_p \approx 0.15h$ and (*e*) $y_m = y_p \approx 0.2h$; (*b*,*d*,*f*) $\gamma_w^2$ spectra of $T_{np}^{'+}$ for the case Ma15Re20K when (*b*) $y_m = y_p \approx 0.1h$, (*d*) $y_m = y_p \approx 0.15h$ and (*f*) $y_m = y_p \approx 0.2h$. The dashed oblique lines in the panels denote $\lambda_x = \lambda_z$, and the dashed transverse and the vertical lines denote $\lambda_z = 2y_p$ and $\lambda_x = 10y_p$, respectively.

where $\langle \exp(q\phi_L) \rangle$ is the momentum generation function, $q$ is a real number, which can be chosen optionally, $s(q) = C_1 \ln\langle \exp(qa) \rangle$ is called anomalous exponent, $C_1$ is a constant and $a$ is a random additive, which represents the footprint of $\phi$ in the near-wall region generated by the attached eddies at a given wall-normal height. The parameter $q$ in the momentum generation function serves as a 'controller' to highlight different components of $\phi_L$ (Yang, Marusic & Meneveau 2016). To be specific, a positive $q$ emphasizes the positive component of $\phi_L$ and *vice versa*. Furthermore, the $n$th-order moment of $\phi_L$ can be derived by (Yang *et al.* 2016)

$$\langle \phi_L^n \rangle = \left. \frac{\partial^n \langle \exp(q\phi_L) \rangle}{\partial q^n} \right|_{q=0}. \tag{4.7}$$

This relationship will be employed in § 5.1.

If $a$ is a Gaussian variable, the anomalous exponent can be recast as

$$s(q) = C_2 q^2, \tag{4.8}$$

where $C_2$ is another constant. However, an extended self-similarity (ESS) is defined to describe the relationship between $\langle \exp(q\phi_L) \rangle$ and $\langle \exp(q_0\phi_L) \rangle$ (fixed $q_0$)

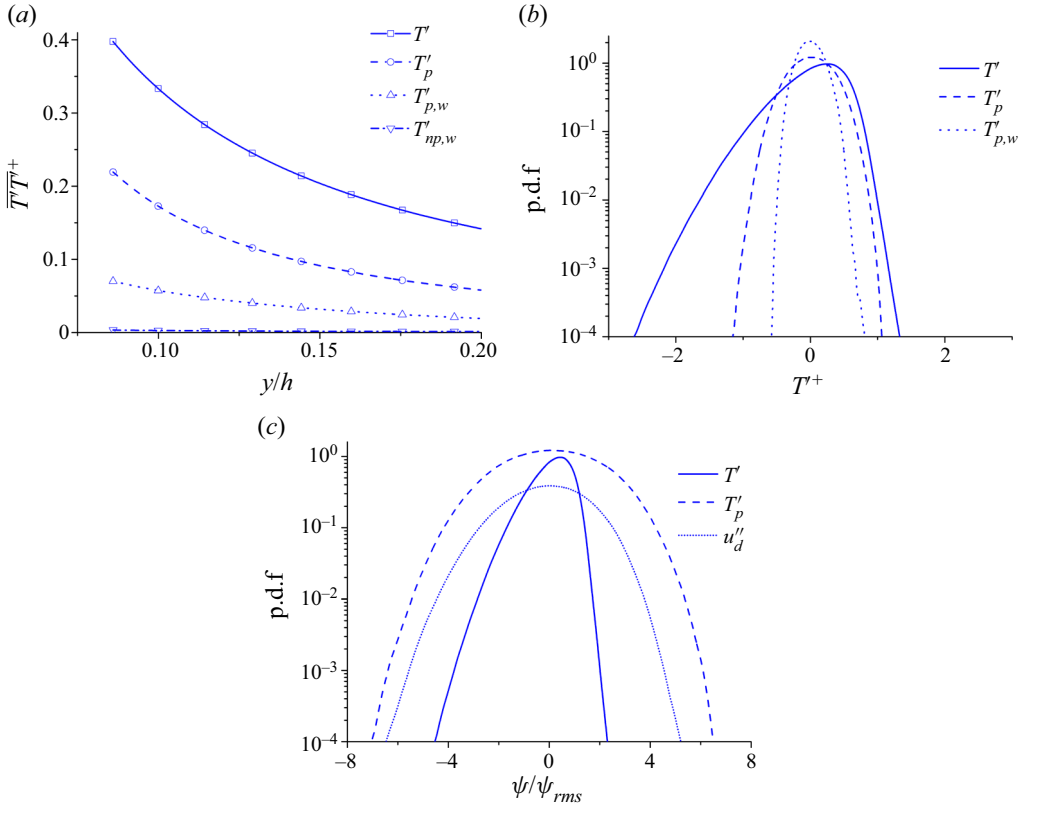


Figure 11. (*a*) Variations of the fluctuation intensities of $T'$, $T'_p$, $T'_{p,w}$ and $T'_{np,w}$ as functions of the wall-normal height $y/h$ in the logarithmic region for the case Ma15Re20K; (*b*) p.d.f.s of the instantaneous $T'^+$, $T'^+_p$ and $T'^+_{p,w}$ at $y/h = 0.1$ for the case Ma15Re20K; (*c*) p.d.f.s of the instantaneous $T'$, $T'_p$ and $u''_d$ at $y/h = 0.1$ for the case Ma15Re20K. Each variable is normalized by its r.m.s. value in panel (*c*). The $\psi$ in the abscissa of panel (*c*) stands for the corresponding variable.

(Benzi *et al.* 1993), i.e.

$$\langle \exp(q\phi_L) \rangle = \langle \exp(q_0\phi_L) \rangle^{\xi(q,q_0)}, \tag{4.9}$$

where $\xi(q, q_0)$ is a function of $q$ (fixed $q_0$). Note that the validity of ESS depends on the hierarchical structures of $\phi$ in the logarithmic region, dominantly. A more detailed derivation of the SSS and the ESS associated with the footprints of the attached eddies can be found in Cheng & Fu (2022*a*).

For the footprints of the temperature fluctuations in supersonic channel flows, they can be obtained by following (2.4) and (2.5) with $T'_\psi = T'_p$. Concurrently, we can further define a moment generation function based on this estimation. It takes the form of

$$G(q, y_p) = \langle \exp(q(T'^+_{p,L}(y_s, y_i) - T'^+_{p,L}(y_p, y_i))) \rangle, \tag{4.10}$$

where $T'^+_{p,L}(y_s, y_i) - T'^+_{p,L}(y_p, y_i)$ is the footprint of $T'^+_p$ generated by the attached eddies with their wall-normal heights varying from $y_s$ to $y_p$, which resembles the $\phi_L$ in (4.6) and (4.9). Here, $T'_{p,L}$ is calculated by an $H_L-$based estimation according to (2.4) and (2.5). As per the hierarchical attached eddies in high-Reynolds-number wall turbulence,

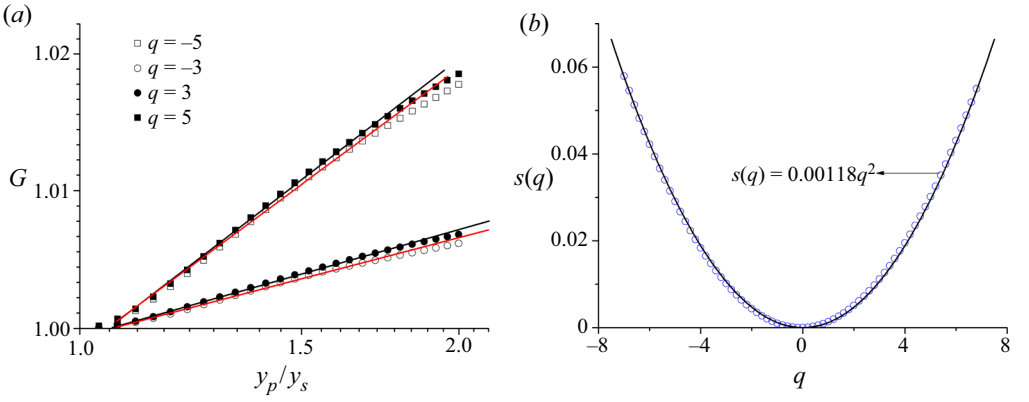


Figure 12. (*a*) The variations of $G$ as a function of $y_p/y_s$ for $q = \pm 5$ and $q = \pm 3$; (*b*) anomalous exponent $s(q)$ as a function of $q$. The line in panel (*b*) is a quadratic fit. The data are taken from the case Ma15Re20K.

$T^{'+}_{p,L}(y_s, y_i)$ is the superposition at $y_i$ contributed from the wall-coherent motions with their heights larger than $y_s$. Thus, the difference value $T^{'+}_{p,L}(y_s, y_i) - T^{'+}_{p,L}(y_p, y_i)$ can be interpreted as the superposition contribution generated by the wall-coherent eddies with their wall-normal heights within $y_s$ to $y_p$ (Cheng & Fu 2022*a*; Cheng *et al.* 2022). The above process is not applied to $T^{'+}_{np}$, because we have verified that $T^{'+}_{np}$ is not coherent with the near-wall flow and does not bear a footprint (see figures 10 and 11*a*).

Figure 12(*a*) shows the variations of $G$ as a function of $y_p/y_s$ for $q = \pm 5$ and $q = \pm 3$. Power-law behaviours can be found in the interval $1.1 \leq y_p/y_s \leq 1.8$ for both positive and negative $q$, justifying the validity of SSS, i.e. (4.6). This observation highlights that the superpositions of wall-attached $T'$ on the wall surface follow an additive process. Additionally, the positive and negative components of $T^{'+}_{p,L}(y_s, y_i) - T^{'+}_{p,L}(y_p, y_i)$ are comparatively symmetrical (for lower Mach number, the asymmetries are more obvious, see § 5.1). Furthermore, in an incompressible channel flow, the asymmetries between the footprints of the high-speed and the low-speed $u'$ motions are quite evident, see Cheng & Fu (2022*a*). Other $q$ values yield similar results and are not shown here for brevity. The anomalous exponent $s(q)$ can be obtained by fitting the range $1.1 \leq y_p/y_s \leq 1.8$, where both positive and negative $q$ display good power-law scalings. Figure 12(*b*) shows the variation of the anomalous exponent $s(q)$ as a function of $q$. The solid line denotes the quadratic fit within $-1 \leq q \leq 1$. It can be seen that the variation of $s(q)$ still follows a quadratic law at large $|q|$. Moreover, the skewness and flatness of the footprints of $T'$ generated by the attached eddies across the whole logarithmic region are $-0.22$ and 3.11 (the counterparts of $u'$ in an incompressible turbulent channel flow at $Re_\tau = 2003$ are 0.05 and 2.91 (Cheng & Fu 2022*a*)). These observations signify that the near-wall heat flux generated by the attached eddies at a given wall-normal height can also be simply treated as a Gaussian variable for modelling purposes (though a little super-Gaussian) at this $M_b$. In the next section, we will discuss the Mach number effects on these statistics.

Different from SSS, ESS only relies on the hierarchical structures of $T'$ in the logarithmic region. Figure 13(*a*,*b*) shows the ESS scalings for $q_0 = -2$ and $q_0 = 2$, respectively. As seen, ESS holds for the entire logarithmic region. This observation suggests that the generation of the near-wall heat flux by the multi-scale logarithmic motions obeys an additive process.

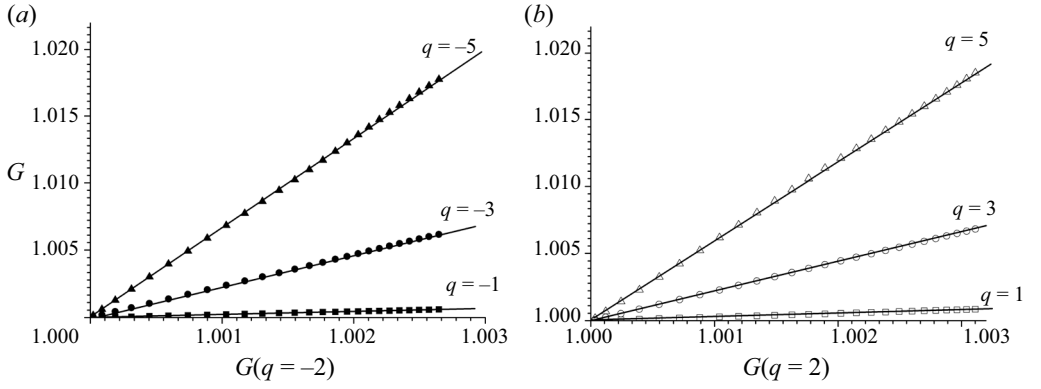


Figure 13. The variations of (*a*) $G(q)$ as functions of $G(-2)$ for $q = -1, -3, -5$; (*b*) $G(q)$ as functions of $G(2)$ for $q = 1, 3, 5$. Both vertical and horizontal axes in panels (*a*) and (*b*) are plotted in logarithmic form. The data are taken from the case Ma15Re20K.

In summary, in the logarithmic region, the $T'$ motions are found to be linearly coupled with the streamwise velocity fluctuations at the scales which are corresponding to the attached eddies and the VLSMs. The wall-attached structures contribute nearly 34 % of $\overline{T_p'^2}^+$ in the logarithmic region (equal to 15 % of $\overline{T'^2}^+$). By dissecting their footprints, it is demonstrated that $T'$ motions in the logarithmic region are organized as hierarchical structures and can be described by the AEM. This observation is consistent with some recent studies on the temperature field in compressible wall turbulence (Cheng & Fu 2022*b*; Yu *et al.* 2022; Yuan *et al.* 2022). Moreover, we further reveal that their footprints are non-intermittent and Gaussian in a supersonic channel flow.

#### 4.1.4. *Outer region ($y_m = y_p \approx 0.85h$)*

As $y_m(y_p)$ moves into the outer region, the linear coupling between $u_d''$ and $T'$ becomes weaker. This phenomenon is more obvious at the outer region near the channel centre. This is to be anticipated since $u_d''$ and $T'$ are only linearly coupled at larger scales as $y_m(y_p)$ increases, as per our study above. In this subsection, we further shed light on this fact. We only show the results of the case Ma15Re20K due to its relatively higher Reynolds number.

Figure 14(*a*,*b*) illustrate the $\gamma_c^2$ and $R_{pm}$ spectra for $y_m = y_p \approx 0.85h$, respectively. Intriguingly, the two spectra are only non-trivial at $\lambda_z > 1h$ and $\lambda_x > 2h$, which are significantly different from those in the logarithmic and the near-wall regions. Only VLSMs of $T'$ and $u_d''$ are weakly coupled. Another interesting observation which deserves attention is that these coupled motions are not isotropic as the scale characteristics of $T'^+$ in the outer region (see figure 4*f*). In contrast, they resemble the scale characteristics of $u_d''^+$ in the outer region (see figure 4*e*). In other words, $T_p'^+$ is 'passive' in shaping their scale properties. Figure 15(*a*,*b*) display the instantaneous $T'^+$ and $T_p'^+$ for $y_m = y_p \approx 0.85h$, respectively. Apparently, the motions of $T_p'^+$ emerge like those of $u_d''^+$ (figure 3*e*) rather than $T'^+$.

All in all, for the first branch of the linear-model-based analysis, i.e. $y_p = y_m$, the applicability of SLSE depends on the wall-normal location in the boundary layer and is

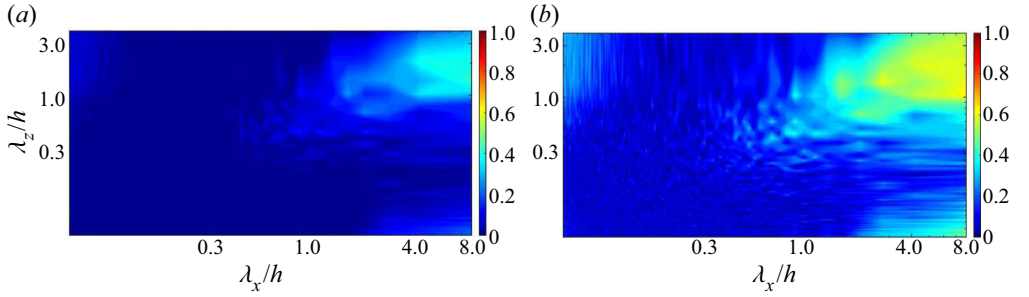


Figure 14. (*a*) The $\gamma_c^2$ spectrum when $y_m = y_p \approx 0.85h$ for the case Ma15Re20K; (*b*) $R_{pm}$ spectrum when $y_m = y_p \approx 0.85h$ for the case Ma15Re20K.

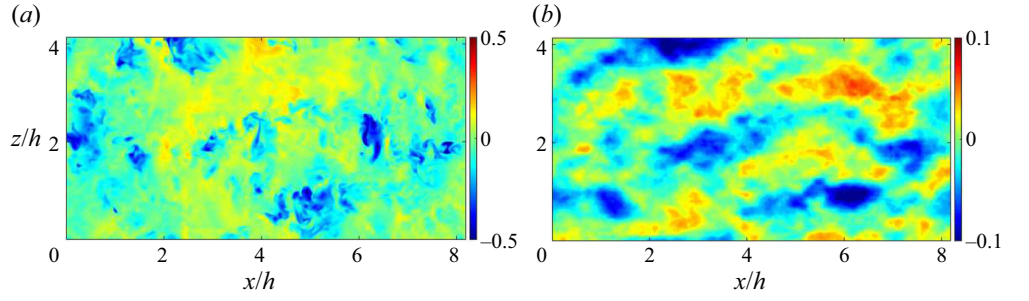


Figure 15. (*a*) Top view of the instantaneous $T'^+$ field when $y_m = y_p \approx 0.85h$; (*b*) top view of the instantaneous $T_p'^+$ field when $y_m = y_p \approx 0.85h$. The data are taken from the case Ma15Re20K.

closely related to the energy-containing motions residing in it. In the next section, we are dedicated to another branch, namely $y_p \neq y_m$.

### 4.2. *Linear-model-based analysis with* $y_m \neq y_p$

For this branch of the linear-model-based analysis, we only consider one realization, i.e. $y_m > y_p$ with $y_m$ being in the logarithmic region. That is to say, what we pursue here is the estimation of the $T'$ in the near-wall region by invoking the $u_d''$ in the logarithmic region through the linear model. This study bears some practical significance. For example, it may be a guideline for the reconstruction of the temperature signals in the near-wall region by employing limited velocity signals recorded by a hot-wired probe in the logarithmic region. Hereafter, we adopt the case Ma15Re20K, and fix $y_m^*$ as 80, $0.2h^*$ and $3.9\sqrt{Re_\tau^*}$ (namely the centre of the logarithmic layer (Mathis, Hutchins & Marusic 2011), $y_m \approx 0.14h$ for Ma15Re20K). Concurrently, $y_p$ varies from the viscous sublayer to $y_m$. The reason we only use the case Ma15Re20K is due to its relatively higher Reynolds number than other cases.

Figure 16(*a*) shows the profiles of $\overline{T_p'^2}^+$ within the range $0 < y_p^* < y_m^*$ and the profile of $\overline{T'^2}^+$ is also included for comparison. Only a fraction of temperature fluctuations can be recovered by the linear model with inputs $u_d''$ from the logarithmic region. It is noted that the wall-normal location of the peaks of $\overline{T_p'^2}^+$ is identical to that of $\overline{T'^2}^+$ regardless of the locus of $y_m^*$, namely $y_p^* \approx 10$. This is under expectation, since the temperature fluctuations have more energy at this wall-normal position indeed. Figure 16(*b*) illustrates

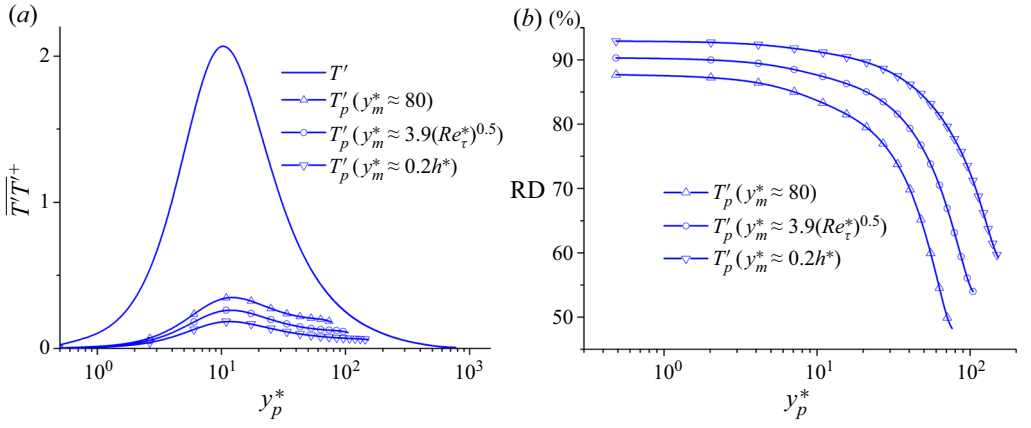


Figure 16. (*a*) Profiles of $\overline{T'^2_p}^+$ within the range $0 < y^*_p < y^*_m$, and the profile of $\overline{T'^2}^+$ is also included for comparison; (*b*) variations of RD as functions of $y^*_p$. The data are taken from the case Ma15Re20K, and $y^*_m \approx 80$, $3.9\sqrt{Re^*_\tau}$ and $0.2h^*$.

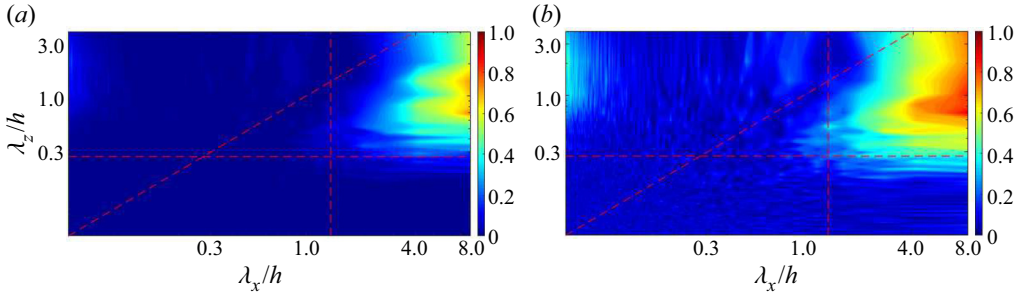


Figure 17. (*a*) The $\gamma^2_c$ spectrum when $y^*_p = 10$ for the case Ma15Re20K; (*b*) $R_{pm}$ spectrum when $y^*_p = 10$ for the case Ma15Re20K. Here, $y^*_m$ is set as $3.9\sqrt{Re^*_\tau}$. The dashed oblique lines in the panels denote $\lambda_x = \lambda_z$, and the dashed transverse and the vertical lines denote $\lambda_z = 2y_p$ and $\lambda_x = 10y_p$, respectively.

the variations of RD as functions of $y^*_p$. Only 10 % of $\overline{T'^2}^+$ can be captured by the linear model in the viscous sublayer. This ratio increases monotonously when $y_p$ approaches $y_m$.

Figure 17(*a*,*b*) shows the $\gamma^2_c$ and $R_{pm}$ spectra at $y^*_p \approx 10$ with $y^*_m \approx 3.9\sqrt{Re^*_\tau}$, respectively. The streamwise and spanwise length scales in the two figures are scaled in the outer unit rather than viscous unit, because the magnitudes of $\gamma^2_c$ and $R_{pm}$ are observed to be non-negligible only at a large-scale range. Comparing with the $\gamma^2_w$ spectrum of $T'_p$ displayed in figure 10(*c*) when $y_p = y_m \approx 0.15h$, it is not difficult to find that the $\gamma^2_c$ spectrum here bears similar scale characteristics. It suggests that only the wall-attached superposition components contributed by the motions at $y_m$ are identified at $y_p$ by the linear model. Figure 17(*b*) also shows akin results.

Figure 18(*a*) further shows the p.d.f.s of $T'^+_p(y_m \neq y_p)$ at $y^*_p \approx 10$ with $y^*_m \approx 3.9\sqrt{Re^*_\tau}$, and the counterparts of $T'^+(y^* = 10)$ and $T'^+_p(y^*_m = y^*_p \approx 10)$ are also included for comparison. Comparing with the other two profiles, the p.d.f. of $T'^+_p(y_m \neq y_p)$ is rather symmetric with invisible extreme events. It signifies that in the near-wall region, only the long temperature streaks with mild fluctuation intensities have linkages with the

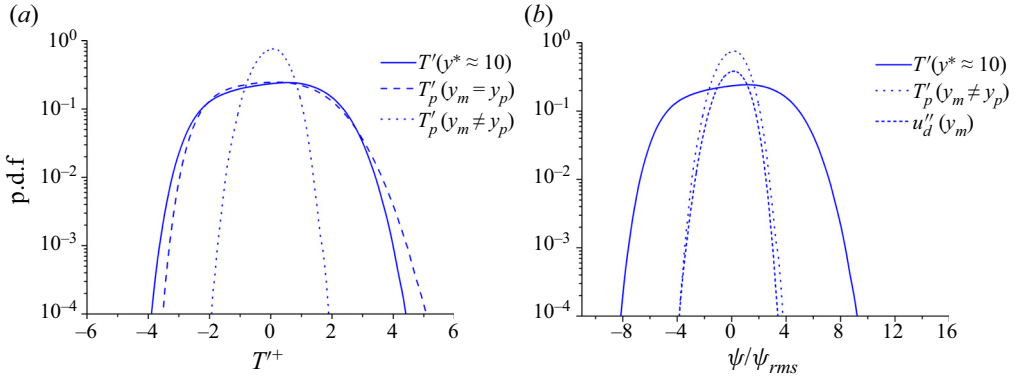


Figure 18. (*a*) The p.d.f.s of $T_p'^{+}(y_m \neq y_p)$ at $y_p^* \approx 10$ with $y_m^* \approx 3.9\sqrt{Re_\tau^*}$, and the counterparts of $T'^{+}(y^* = 10)$ and $T_p'^{+}(y_m^* = y_p^* \approx 10)$ are also included for comparison. (*b*) The p.d.f.s of $T'_p(y_m \neq y_p)$ at $y_p^* \approx 10$ with $y_m^* \approx 3.9\sqrt{Re_\tau^*}$, $T'(y^* = 10)$ and $u''_d(y_m)$. Each variable is normalized by its r.m.s. value in panel (*b*). The $\psi$ in the abscissa of panel (*b*) stands for the corresponding variable. The data are taken from the case Ma15Re20K.

motions in the logarithmic region. Furthermore, the near-wall flow should be given more consideration to control the extreme thermal events on the wall surface in supersonic wall turbulence, because, according to the results shown here, the intensities of the superposition components contributed by the motions populating the logarithmic and the outer regions are not that large indeed. Figure 18(*b*) displays the p.d.f.s of $T'(y^* \approx 10)$, $T'_p(y_m \neq y_p)$ at $y_p^* \approx 10$ and $u''_d(y_m)$ with $y_m^* \approx 3.9\sqrt{Re_\tau^*}$. Even though $y_m \neq y_p$, the p.d.f. shape of the predicted $T'_p$ at $y_p$ still conforms to that of $u''_d$ at $y_m$.

## 5. Discussion

### 5.1. *Mach number effects*

In this subsection, we are dedicated to shedding light on the Mach number effects on the linear coupling between $u''_d$ and $T'$ by analysing the subsonic cases listed in table 1. We acknowledge that the DNS data with a higher Mach number (for example, $M_b = 3.0$) are needed for conducting a more comprehensive study on this problem. However, the DNS of supersonic channel flows at both high Mach number and Reynolds number demands huge computational costs. A more extensive investigation of the Mach number effects will be carried out when the database is available.

Following the above manner, we start by taking the situation $y_m = y_p$ into consideration. Figure 19(*a*,*b*) shows the variations of RD for all cases as functions of $y_p/h$ and $y_p^*$, respectively. The supersonic cases are illustrated by solid lines, whereas the subsonic ones by dashed lines. Apart from the two cases with $Re_\tau^* \approx 160$, the profiles of RD with similar $Re_\tau^*$ overlap with each other. The exceptions of the two cases may result from the low-Reynolds-number effects. It suggests that the Mach number has negligible effects on the linear coupling between $u''_d$ and $T'$. It is the Reynolds number $Re_\tau^*$ rather than Mach number that acts as a key similarity parameter in constructing their coupling. This observation is consistent with our previous work on the scale characteristics of the energy-containing motions in compressible channel flows (Cheng & Fu 2022*b*).

For $y_p = y_m$ in the logarithmic region, all the wall-attached temperature streaks are found to be contained in $T'_p$ (not shown here), and the SSS (4.6) is examined and shown in figure 20 by analysing the case Ma08Re17K. Figure 20(*a*) shows the variations of $G$ as

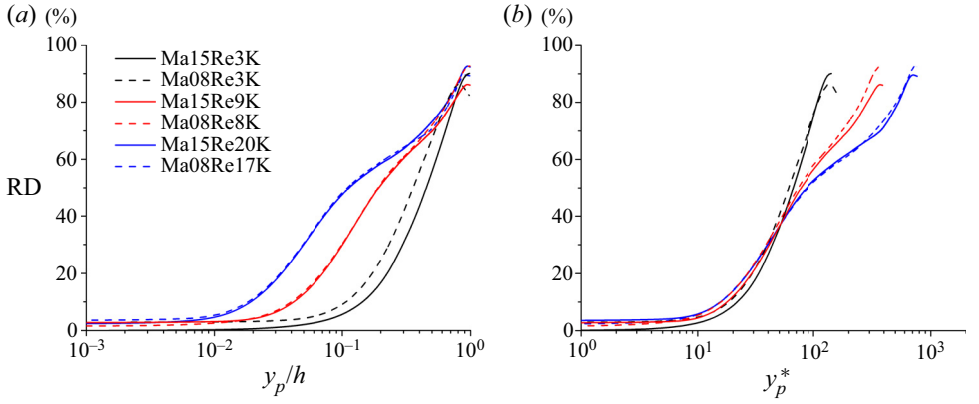


Figure 19. (*a*) Relative deviations (RDs) as functions of $y_p/h$ for all the cases; (*b*) relative deviations (RDs) as functions of $y_p^*$ for all the cases. Here, $y_p$ equals to $y_m$ for these cases under consideration.

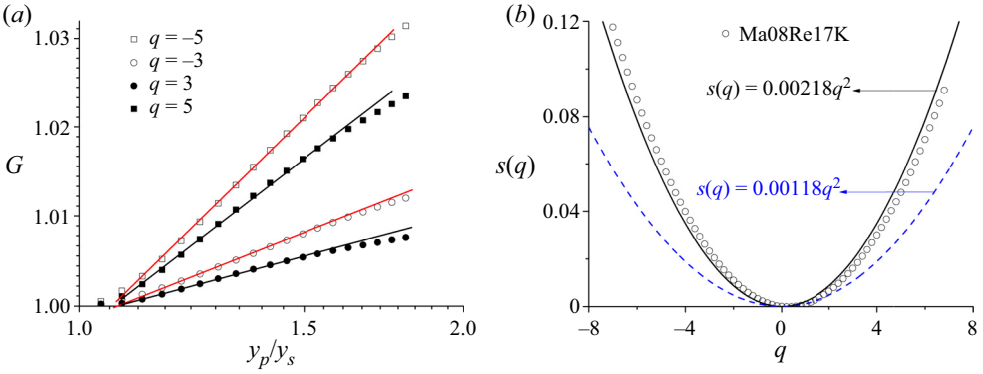


Figure 20. (*a*) The variations of $G$ as a function of $y_p/y_s$ with $q = \pm 5$ and $q = \pm 3$ for Ma08Re17K; (*b*) anomalous exponent $s(q)$ as a function of $q$ for Ma08Re17K. The solid line in panel (*b*) is a quadratic fit, and the dashed line is the result of the supersonic case Ma15Re20K, which is included here for comparison.

a function of $y_p/y_s$ for $q = \pm 5$ and $q = \pm 3$. It is particularly noteworthy that power-law behaviours can be found in the interval of $1.1 \leq y_p/y_s \leq 1.6$ with discernible differences between $G(q)$ and $G(-q)$. By comparing with figure 12(*a*), it can be conjectured that the enlargement of the Mach number leads to the disappearance of the asymmetric characteristics between the positive and the negative footprints of $T'$ generated by the attached eddies.

This assertion can also be validated by examining the variational tendency of the anomalous exponent $s(q)$ (figure 20*b*). The profile of $s(q)$ of Ma08Re17K is not that symmetric with regards to $q$ and has an optimal $C_2 \approx 0.00218$, in contrast to the result of Ma15Re20K (see figure 12*b*). It indicates that the distribution of near-wall heat flux generated by the attached eddies at a given wall-normal height deviates from the Gaussian distribution slightly at this Mach number. This scenario is altered by the increased compressibility of the supersonic flows. Moreover, it can also be noticed that the optimal $C_2$ of Ma08Re17K is remarkably different from that of Ma15Re20K (see blue dashed line in figure 20*b*). It strongly suggests that there is a striking difference in the Reynolds number dependence of the wall-heated flux fluctuation intensities at different $M_b$ for compressible channel flows. If we acknowledge that the Reynolds number dependence of wall heated

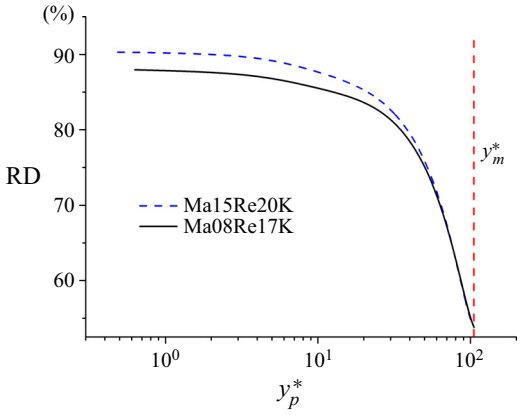


Figure 21. Variations of RD as functions of $y_p^*$ for the cases Ma08Re17K and Ma15Re20K. Here, $y_m^* \approx 3.9\sqrt{Re_\tau^*}$ (the vertical line) and $0 < y_p^* < y_m^*$.

flux fluctuation intensity can be ascribed to the superposition of the self-similar attached eddies (obviously, this is not true), the variational tendency of the temperature fluctuation intensity in the viscous sublayer contributed by the attached eddies can be predicted by (Yang *et al.* 2016; Cheng & Fu 2022*a*)

$$\left.\frac{\partial^2 G(q, y_p)}{\partial q^2}\right|_{q=0} \sim 2C_2 \ln(y_p/y_s). \tag{5.1}$$

Unequal $C_2$ for subsonic and supersonic flows indicates their different variational tendencies with respect to $\ln(y_p/y_s)$. It underlines the fact that it is rather difficult to formulate the Reynolds number dependence of the wall heated flux at different Mach numbers by a unified formula without taking Mach number effects into account. For $y_p = y_m$ in the outer region close to the channel centre, the effectiveness of the linear model is limited. For sake of brevity, these results are not shown here.

At last, let us turn our attention to another situation with $y_m \neq y_p$. Similarly, $y_m^*$ is fixed as $3.9\sqrt{Re_\tau^*}$ ($y_m \approx 0.14h$ for Ma08Re17K), the centre of the logarithmic layer, and $y_p$ varies from the viscous sublayer to $y_m$. Figure 21 compares the variations of RD as a function of $y_p^*$ for Ma08Re17K and Ma15Re20K. For $y_p^* < 50$, the RD of Ma15Re20K is larger than that of Ma08Re17K, whereas they overlap with each other for $y_p^* > 50$. It may imply that the compressibility lessens the linkages between the near-wall temperature field and the energy-containing motions populating the logarithmic region slightly. The higher mean-temperature gradient of the supersonic case near the wall may preclude the permeation of the wall-attached eddies. Whether it holds or not at larger Mach number deserves further investigations.

### 5.2. *Strong Reynolds analogy: a heuristic study*

By far, we have shown that the temperature and the velocity fluctuations are highly linked with each other through the prism of the multi-scale energy-containing eddies. However, the SRA (1.1), which is deduced from the momentum and the energy equations with some ideal hypotheses, indicates this interconnection from the mathematical statistics side (Morkovin 1962). A question may be raised, e.g. can the present study be instructive to

unravel the physical significance behind the SRA? In this subsection, we try to answer this question in a heuristic way.

Gaviglio (1987) observed that, for a compressible boundary layer, the intensities of the velocity and the temperature fluctuations carried by large-scale eddies are in direct proportion to the gradients of their mean quantities. Additionally, their corresponding ratios are positively related to the velocity length scale ($\ell_u$) and the temperature length scale ($\ell_T$), respectively. In a statistical manner, this relationship can be expressed by

$$a\sqrt{\overline{T'^2}}/\partial_y\bar{T} = \sqrt{\overline{u'^2}}/\partial_y\bar{u}, \tag{5.2}$$

where $a = \ell_u/\ell_T$, namely the ratio between the velocity and the temperature length scales. Equation (5.2) can be further cast as

$$\frac{\sqrt{\overline{T'^2}}/\bar{T}}{(\gamma-1)M^2\sqrt{\overline{u'^2}}/\bar{u}} = \frac{1}{a(1-\partial\bar{T}_t/\partial\bar{T})}, \tag{5.3}$$

where $\bar{T}_t$ denotes the mean total temperature. Gaviglio (1987) and Rubesin (1990) modelled $a = 1$ and $a = 1.34$, which are denoted as GSRA and RSRA hereafter, respectively. Huang *et al.* (1995) further pointed out that $a$ should be strictly identical to the so-called turbulent Prandtl number $Pr_t$, whose definition takes the form of

$$Pr_t = \frac{\overline{\rho v'u'}\partial_y\bar{T}}{\overline{\rho v'T'}\partial_y\bar{u}}. \tag{5.4}$$

We denote this version of SRA as HSRA hereafter. The performance of HSRA has been reported to be excellent not only in wall-cooling turbulent channel flows, but also in the turbulent boundary layers with different wall heated conditions, varying Mach numbers and thermochemical non-equilibrium effects (Huang *et al.* 1995; Duan, Beekman & Martin 2010, 2011; Fu *et al.* 2021; Huang *et al.* 2022; Passiatore *et al.* 2022). Additionally, Zhang *et al.* (2014) proposed another definition of the turbulent Prandtl number, i.e.

$$Pr_t^\star = \frac{\overline{(\rho v)'u'}\partial_y\bar{T}}{\overline{(\rho v)'T'}\partial_y\bar{u}}. \tag{5.5}$$

The modified HSRA with this new definition of the turbulent Prandtl number yields even better results than the original HSRA (Zhang *et al.* 2014). We denote this version of SRA as MHSRA hereafter.

To connect the present linear coupling study with the SRA, here, we make three propositions regarding the multi-scale interactions in compressible turbulence. First, the mean flow field only controls the dynamics of the large-scale energy-containing eddies in the turbulent boundary layers. This assertion has been fully supported by abounding studies, e.g. Goto, Saito & Kawahara (2017), Lozano-Durán *et al.* (2021), to name a few. Second, the large-scale energy-containing eddies which interact with the mean flow field are chiefly the carriers that sustain the linear coupling between $u_d''$ and $T'$. This proposition is also rational, because our study above shows that $u_d''$ and $T'$ are linearly coupled at these scales. Third, the small-scale eddies that are not responsible for the linear coupling between $u_d''$ and $T'$ have negligible effects in determining the scale ratio $a$ in (5.2). After all, the physical model of Gaviglio (1987) is a description of the dynamics of the large-scale eddies.

On the basis of the above understanding, $T'_p(y_m = y_p)$ can be considered as the temperature fluctuations carried by the large-scale energy-containing eddies at $y_p$ which interact with the mean flow field. Apparently, the component of $u''_d$ which is carried by them (denoted as $u''_{d,p}$) and interacts with the mean flow field should also be provided. Thus, we introduce another kernel function $H_u$, which reads as

$$H_u(\lambda_x, \lambda_z; y_m, y_p) = \frac{\langle \hat{u}''_d(\lambda_x, \lambda_z; y_p)\breve{\hat{T}}'(\lambda_x, \lambda_z; y_m)\rangle}{\langle \hat{T}'(\lambda_x, \lambda_z; y_m)\breve{\hat{T}}'(\lambda_x, \lambda_z; y_m)\rangle}, \tag{5.6}$$

and $u''_{d,p}$ can be estimated by

$$u''_{d,p}(y_m, y_p) = F^{-1}_{x,z}\{H_u(\lambda_x, \lambda_z; y_m, y_p)F_{x,z}[T'(y_m)]\}, \tag{5.7}$$

where $y_m = y_p$. The intensities of $u''_{d,p}$ and $T'_p$ truly reflect the interactions dominated by the large-scale eddies according to the physical picture depicted by Gaviglio (1987). Hence, the scale ratio $\ell_u/\ell_T$ can be estimated by a modified version of (5.2) which takes the density variation effects into consideration, i.e.

$$a_\rho = \frac{\sqrt{\overline{u''^2_{d,p}}}/\partial_y\overline{u_d}}{\sqrt{\overline{T'^2_p}}/\partial_y\bar{T}}, \tag{5.8}$$

where $\overline{u_d} = \overline{\sqrt{\rho}u}$ is the density-weighted mean streamwise velocity, which corresponds to the definition of $u''_d$. Hereby, by invoking $u''_{d,p}$ and $T'_p$, (5.8) genuinely establishes the relationship between the linearly coupled interactions and the physical picture of the SRA.

Figure 22(*a–c*) shows the variations of $a_\rho$, $Pr_t$ and $Pr^*_t$ for all cases, respectively. It can be seen that there is a negligible difference between $Pr_t$ and $Pr^*_t$. This is under expectation, since Zhang *et al.* (2014) pointed out that these two definitions only display discernible differences at large Mach numbers. The empirical formula given by Abe & Antonia (2017) for incompressible flow is included in figure 22(*b*,*c*) for comparison. This formula is in accordance with the DNS results for $y/h > 0.3$, except for the two low-Reynolds-number cases ($Re^*_\tau \approx 160$). The wall-normal distributions of $Pr_t$ and $Pr^*_t$ in compressible channel flows are akin to those in incompressible flows with $Pr$ close to unity (Pirozzoli *et al.* 2016; Abe & Antonia 2017, 2019). Furthermore, it is interesting to find that the magnitudes of $a_\rho$ are very close to those of $Pr_t$ and $Pr^*_t$, and not sensitive to the Mach number and Reynolds number. It highlights a new and underlying physical significance of $Pr_t$. That is, $Pr_t$ is also a precise indicator of the linear coupling between the velocity and the temperature fields. However, $Pr_t$ is defined as the ratio between the momentum and the heat transfer eddy diffusivity. This definition in turn implies the origin of the linear coupling between the two fields, that is, the similarity between the momentum and the heat transfer. Moreover, it also suggests that the propositions affirmed above are logical. Figure 22(*d*) compares the results of GSRA, RSRA, HSRA, MHSRA and the present study (using $a_\rho$ in (5.8)) by plotting the right-hand side of (5.3) ($R_H$) using the case Ma15Re3K. Other cases show similar results and are not shown here. It can be seen that the result of the present study is close to that of HSRA and MHSRA, which further evidences the similarity among the scale ratio $a_\rho$ , $Pr_t$ and $Pr^*_t$.

Before closing this section, it may be worth making a comment on the comparison with the incompressible flow and the underlying physical relevance. The decreasing magnitude of $Pr_t$ in incompressible wall turbulence is essentially associated with the unmixedness

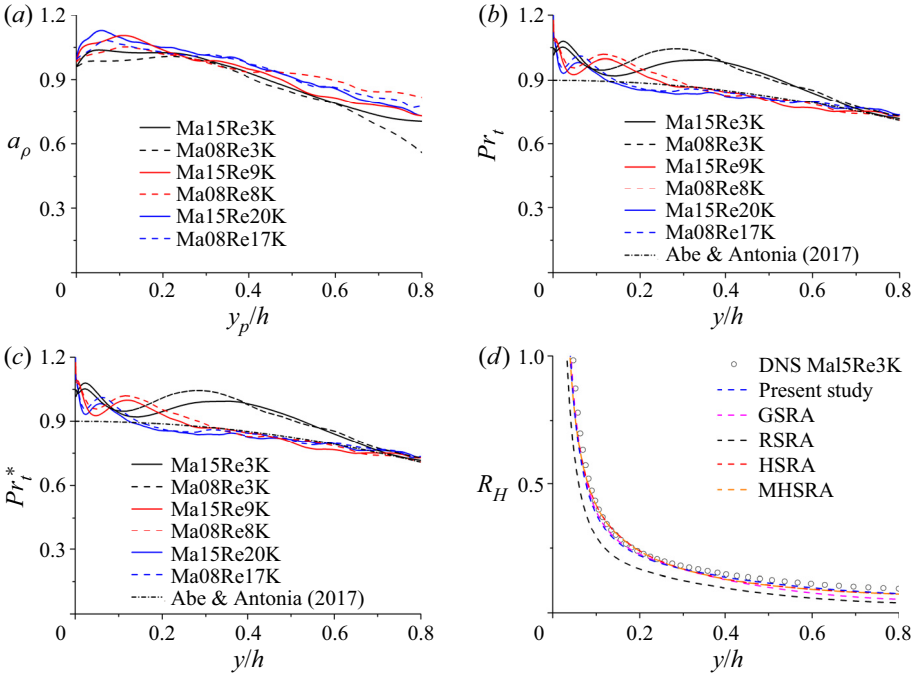


Figure 22. The variations of (*a*) $a_\rho$ as a function of $y_p/h$ for all cases; (*b*) $Pr_t$ as a function of $y/h$ for all cases; (*c*) $Pr_t^*$ as a function of $y/h$ for all cases; (*d*) comparisons of various SRA predictions by using the case Ma15Re3K. The empirical formula $Pr_t = 0.9 - 0.3(y/h)^2$ given by Abe & Antonia (2017) for incompressible flow is included in panels (*b*) and (*c*) for comparison.

of the scalar (Guezennec, Stretch & Kim 1990; Antonia *et al.* 2009; Pirozzoli *et al.* 2016; Abe & Antonia 2019). The $Pr_t$ and $Pr_t^*$ obtained from the compressible channel flows in the present study also diminish in the outer region and show $(y/h)^2$ dependence. This observation indicates that the unmixedness of $T'$ also exists in supersonic and subsonic wall turbulence. Our analyses in this subsection may give some new insights on this phenomenon. The unmixedness is highly linked with the degenerated coupling between the velocity and the temperature fields in the outer region. Moreover, we conjecture that the coupling between the velocity and the temperature fields largely results from the transport effect, rather than a genuine dynamical interaction between the energy and momentum equations, at least within the cases under scrutiny, because there is a remarkable similarity between $a_\rho$, $Pr_t$ in compressible channel flows and $Pr_t$ in incompressible cases. For incompressible turbulence, there is no dynamical interaction between the energy and momentum equations, and $T'$ acts as a passive scalar purely. Hence, it is sensible to hypothesize that the transport effect, which exists in both incompressible and compressible wall turbulence, is the key driving mechanism of the coupling. Whether this scenario will be altered in wall turbulence at larger Mach numbers needs deeper investigations.

## 6. Concluding remarks

In the present study, we adopt a linear model, i.e. SLSE, to dissect the coupling between the velocity and the temperature fields in compressible turbulent channel flows by using DNS data from low to medium Reynolds numbers. The conclusions are summarized below.

(a) In the near-wall region, the two fields are highly coupled and only the extreme thermal events cannot be captured by SLSE.

(b) In the logarithmic region, the $T'$ motions are found to be linearly coupled with the streamwise velocity fluctuations at the scales which correspond to the attached eddies and the VLSMs, namely $\lambda_x > \lambda_z$, $\lambda_x > 10y_p$ and $\lambda_z > 2y_p$. It is also demonstrated that the $T'$ motions in the logarithmic region are organized as hierarchical structures and can be described by the celebrated attached-eddy model. Similar to the behaviour of $u'$, their footprints on the near-wall region can be treated as a Gaussian variable.

(c) In the outer region, the two fields are linearly coupled only at the scales corresponding to VLSMs. Only a fraction of temperature fluctuations can be recovered by SLSE.

(d) The effectiveness of the linear model is found to be insensitive to the compressibility. It is the Reynolds number rather than Mach number that acts as a key similarity parameter in constructing $u$–$T$ coupling. However, the enlargement of the Mach number leads to the disappearance of the asymmetries between the positive and the negative footprints of $T'$ generated by the attached eddies.

(e) The turbulent Prandtl number $Pr_t$ has been shown to be a precise indicator of the linear coupling between the two fields. It also suggests that their coupling is ascribed to the similarity between the momentum and the heat transfer in compressible wall turbulence.

In our opinion, the most important contribution of the present study is the framework built to analyse the multi-physics coupling in complex compressible wall-bounded turbulence. Such a technology is comparatively mature in studying incompressible wall turbulence, but rarely been adopted to inspect the more complex compressible flows. In fact, the multi-physics coupling is more prominent in compressible wall turbulence than incompressible flows to some extent. For example, very recently, several studies have reported that the alterations of the wall thermal boundary condition can remarkably modify the temperature and velocity streaks in supersonic/hypersonic turbulent boundary layers (Hirai *et al.* 2021; Cogo *et al.* 2022; Huang *et al.* 2022). Hence, the present study can provide an effective tool to quantify these variations. However, it should be accentuated that the uncoupled motions are found to be responsible for the extreme thermal events in the near-wall and the logarithmic regions. Their dynamics is a worthwhile subject for further investigations.

**Acknowledgements.** C.C. expresses his gratitude to Y. Zhao for helping to plot figure 6 of the present paper.

**Funding.** L.F. acknowledges funding from the Research Grants Council (RGC) of the Government of Hong Kong Special Administrative Region (HKSAR) with RGC/ECS Project (no. 26200222), the funding from Guangdong Basic and Applied Basic Research Foundation (no. 2022A1515011779), and the funding from the Project of Hetao Shenzhen-Hong Kong Science and Technology Innovation Cooperation Zone (no. HZQB-KCZYB-2020083).

**Declaration of interests.** The authors report no conflict of interest.

**Author ORCIDs.**
Cheng Cheng https://orcid.org/0000-0002-7961-793X;
Lin Fu https://orcid.org/0000-0001-8979-8415.

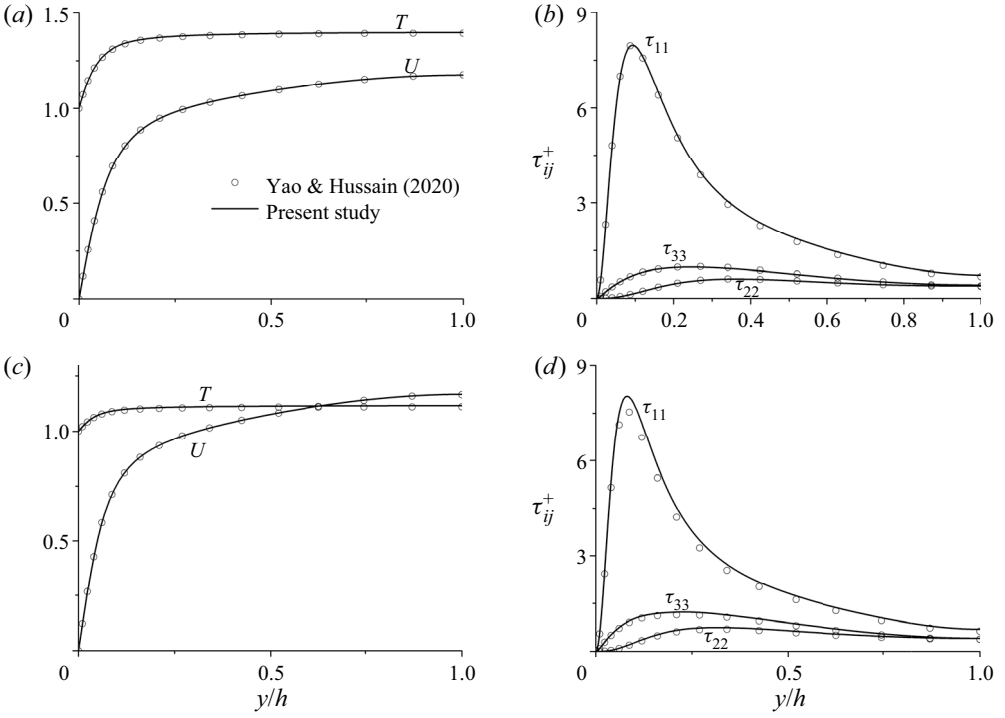


Figure 23. (*a*,*c*) Profiles of mean streamwise velocity and mean temperature for the cases (*a*) Ma15Re3K and (*c*) Ma08Re3K; (*b*,*d*) profiles of the Reynolds stress for the cases (*b*) Ma15Re3K and (*d*) Ma08Re3K.

## Appendix A. Description and validation of DNS database

The DNSs of compressible turbulent channel flows have been conducted with a finite-difference code, by solving the 3-D unsteady compressible Navier–Stokes equations. The convective terms are discretized with a seventh-order upwind-biased scheme and the viscous terms are evaluated with an eighth-order central difference scheme. Time advancement is performed using the third-order strong-stability-preserving (SSP) Runge–Kutta method (Gottlieb, Shu & Tadmor 2001). A constant molecular Prandtl number $Pr$ of 0.72 and a specific heat ratio $\gamma$ of 1.4 are employed. The dependence of dynamical viscosity $\mu$ on temperature $T$ is given by Sutherland's law, i.e.

$$\mu = \mu_0 \frac{T_0 + S}{T + S} \left( \frac{T}{T_0} \right)^{3/2}, \tag{A1}$$

where $S = 110.4K$ and $T_0 = 273.1K$.

The isothermal no-slip conditions are imposed at the top and bottom walls, and the periodic boundary condition is imposed in the wall-parallel directions, i.e. $x$ and $z$ directions. All simulations begin with a parabolic velocity profile with random perturbations superimposed, and uniform temperature and density values. A body force is imposed in the streamwise direction to maintain a constant mass flow rate and a corresponding source term is also added to the energy equation. The code has been validated by previous studies on the energy-containing eddies in quasi-incompressible channel flows and the skin-friction decomposition in supersonic channel flows (Cheng *et al.* 2019; Li *et al.* 2019).

The validations of the cases Ma15Re9K, Ma15Re20K, Ma08Re8K and Ma08Re17K listed in table 1 are provided by Cheng & Fu (2022*b*). Here, we validate the remaining cases, i.e. Ma15Re3K and Ma08Re3K. Figure 23 compares the DNS results of Ma15Re3K and Ma08Re3K with the flow statistics of Yao & Hussain (2020) at identical $Ma_b$ and $Re_b$, respectively. Both the mean quantities and the Reynolds stress $\tau_{ij} = \bar{\rho} R_{ij}$ with $R_{ij} = \widetilde{u_i'' u_j''} = \widetilde{u_i u_j} - \tilde{u}_i \tilde{u}_j$ are compared. All the profiles of the concerned quantities agree reasonably with the previous study and these confirm the accuracy of the present database.

## References


Abe, H. & Antonia, R.A. 2009 Near-wall similarity between velocity and scalar fluctuations in a turbulent channel flow. *Phys. Fluids* **21** (2), 025109.

Abe, H. & Antonia, R.A. 2017 Relationship between the heat transfer law and the scalar dissipation function in a turbulent channel flow. *J. Fluid Mech.* **830**, 300–325.

Abe, H. & Antonia, R.A. 2019 Mean temperature calculations in a turbulent channel flow for air and mercury. *Intl J. Heat Mass Transfer* **132**, 1152–1165.

Abe, H., Antonia, R.A. & Toh, S. 2018 Large-scale structures in a turbulent channel flow with a minimal streamwise flow unit. *J. Fluid Mech.* **850**, 733–768.

Abe, H., Kawamura, H. & Choi, H. 2004*a* Very large-scale structures and their effects on the wall shear-stress fluctuations in a turbulent channel flow up to $Re_\tau = 640$. *Trans. ASME J. Fluids Engng* **126** (5), 835–843.

Abe, H., Kawamura, H. & Matsuo, Y. 2004*b* Surface heat-flux fluctuations in a turbulent channel flow up to $Re_\tau = 1020$ with $P_r = 0.025$ and 0.71. *Intl J. Heat Fluid Flow* **25** (3), 404–419.

Adrian, R.J. 1979 Conditional eddies in isotropic turbulence. *Phys. Fluids* **22** (11), 2065–2070.

Agostini, L. & Leschziner, M. 2014 On the influence of outer large-scale structures on near-wall turbulence in channel flow. *Phys. Fluids* **26** (7), 075107.

Agostini, L. & Leschziner, M. 2019 The connection between the spectrum of turbulent scales and the skin-friction statistics in channel flow at $Re_\tau \approx 1000$. *J. Fluid Mech.* **871**, 22–51.

Ahn, J., Lee, J.H., Lee, J., Kang, J. & Sung, H.J. 2015 Direct numerical simulation of a 30R long turbulent pipe flow at $Re_\tau = 3008$. *Phys. Fluids* **27** (6), 065110.

Antonia, R.A., Abe, H. & Kawamura, H. 2009 Analogy between velocity and scalar fields in a turbulent channel flow. *J. Fluid Mech.* **628**, 241–268.

Baars, W.J., Hutchins, N. & Marusic, I. 2016 Spectral stochastic estimation of high-Reynolds-number wall-bounded turbulence for a refined inner-outer interaction model. *Phys. Rev. Fluids* **1** (5), 054406.

Baars, W.J., Hutchins, N. & Marusic, I. 2017 Self-similarity of wall-attached turbulence in boundary layers. *J. Fluid Mech.* **823**, R2.

Baars, W.J. & Marusic, I. 2020 Data-driven decomposition of the streamwise turbulence kinetic energy in boundary layers. Part 1. Energy spectra. *J. Fluid Mech.* **882**, A25.

Bai, T., Griffin, K.P. & Fu, L. 2022 Compressible velocity transformations for various noncanonical wall-bounded turbulent flows. *AIAA J.* **60**, 4325–4337.

Baidya, R., *et al.* 2019 Simultaneous skin friction and velocity measurements in high Reynolds number pipe and boundary layer flows. *J. Fluid Mech.* **871**, 377–400.

Bendat, J.S. & Piersol, A.G. 2011 *Random Data: Analysis and Measurement Procedures*. John Wiley & Sons.

Benzi, R., Ciliberto, S., Tripiccione, R., Baudet, C., Massaioli, F. & Succi, S. 1993 Extended self-similarity in turbulent flows. *Phys. Rev.* E **48**, R29–R32.

Brun, C., Petrovan, B.M., Haberkorn, M. & Comte, P. 2008 Large eddy simulation of compressible channel flow. *Theor. Comput. Fluid Dyn.* **22** (3), 189–212.

Cebeci, T. & Smith, A. 1976 Analysis of turbulent boundary layers. *J. Appl. Mech.* **75** (15), 46513.

Cheng, C. & Fu, L. 2022*a* Consistency between the attached eddy model and the inner outer interaction model: a study of streamwise wall shear stress fluctuations in a turbulent channel flow. *J. Fluid Mech.* **942**, R9.

Cheng, C. & Fu, L. 2022*b* Large-scale motions and self-similar structures in compressible turbulent channel flows. *Phys. Rev. Fluids* **7** (11), 114604.

Cheng, C. & Fu, L. 2023 A scale-based study of the Reynolds number scaling for the near-wall streamwise turbulence intensity in wall turbulence. *Intl J. Heat Fluid Flow* **101**, 109136.

CHENG, C., LI, W., LOZANO-DURÁN, A. & LIU, H. 2019 Identity of attached eddies in turbulent channel flows with bidimensional empirical mode decomposition. *J. Fluid Mech.* **870**, 1037–1071.

CHENG, C., LI, W., LOZANO-DURÁN, A. & LIU, H. 2020*a* On the structure of streamwise wall-shear stress fluctuations in turbulent channel flows. *J. Fluid Mech.* **903**, A29.

CHENG, C., LI, W., LOZANO-DURÁN, A. & LIU, H. 2020*b* Uncovering townsend wall-attached eddies in low-Reynolds-number wall turbulence. *J. Fluid Mech.* **889**, A29.

CHENG, C., SHYY, W. & FU, L. 2022 Streamwise inclination angle of wall-attached eddies in turbulent channel flows. *J. Fluid Mech.* **946**, A49.

CHO, M., HWANG, Y. & CHOI, H. 2018 Scale interactions and spectral energy transfer in turbulent channel flow. *J. Fluid Mech.* **854**, 474–504.

COGO, M., SALVADORE, F., PICANO, F. & BERNARDINI, M. 2022 Direct numerical simulation of supersonic and hypersonic turbulent boundary layers at moderate-high Reynolds numbers and isothermal wall condition. *J. Fluid Mech.* **945**, A30.

COLEMAN, G.N., KIM, J. & MOSER, R.D. 1995 A numerical study of turbulent supersonic isothermal-wall channel flow. *J. Fluid Mech.* **305**, 159–183.

DEL ÁLAMO, J.C. & JIMÉNEZ, J. 2003 Spectra of the very large anisotropic scales in turbulent channels. *Phys. Fluids* **15** (6), L41–L44.

DEL ÁLAMO, J.C., JIMÉNEZ, J., ZANDONADE, P. & MOSER, R.D. 2004 Scaling of the energy spectra of turbulent channels. *J. Fluid Mech.* **500**, 135–144.

DEL ÁLAMO, J.C., JIMÉNEZ, J., ZANDONADE, P. & MOSER, R.D. 2006 Self-similar vortex clusters in the turbulent logarithmic region. *J. Fluid Mech.* **561**, 329–358.

DESHPANDE, R., MONTY, J.P. & MARUSIC, I. 2019 Streamwise inclination angle of large wall-attached structures in turbulent boundary layers. *J. Fluid Mech.* **877**, R4.

DESHPANDE, R., MONTY, J.P. & MARUSIC, I. 2021 Active and inactive components of the streamwise velocity in wall-bounded turbulence. *J. Fluid Mech.* **914**, A5.

DUAN, L., BEEKMAN, I. & MARTIN, M.P. 2010 Direct numerical simulation of hypersonic turbulent boundary layers. Part 2. Effect of wall temperature. *J. Fluid Mech.* **655**, 419–445.

DUAN, L., BEEKMAN, I. & MARTIN, M.P. 2011 Direct numerical simulation of hypersonic turbulent boundary layers. Part 3. Effect of Mach number. *J. Fluid Mech.* **672**, 245–267.

ENCINAR, M.P. & JIMÉNEZ, J. 2019 Logarithmic-layer turbulence: a view from the wall. *Phys. Rev. Fluids* **4** (11), 114603.

FOYSI, H., SARKAR, S. & FRIEDRICH, R. 2004 Compressibility effects and turbulence scalings in supersonic channel flow. *J. Fluid Mech.* **509**, 207–216.

FU, L., BOSE, S. & MOIN, P. 2022 Prediction of aerothermal characteristics of a generic hypersonic inlet flow. *Theor. Comput. Fluid Dyn.* **36** (2), 345–368.

FU, L., KARP, M., BOSE, S.T., MOIN, P. & URZAY, J. 2021 Shock-induced heating and transition to turbulence in a hypersonic boundary layer. *J. Fluid Mech.* **909**, A8.

GANAPATHISUBRAMANI, B., CLEMENS, N.T. & DOLLING, D.S. 2006 Large-scale motions in a supersonic turbulent boundary layer. *J. Fluid Mech.* **556**, 271–282.

GAVIGLIO, J. 1987 Reynolds analogies and experimental study of heat transfer in the supersonic boundary layer. *Intl J. Heat Mass Transfer* **30** (5), 911–926.

GEROLYMOS, G.A. & VALLET, I. 2014 Pressure, density, temperature and entropy fluctuations in compressible turbulent plane channel flow. *J. Fluid Mech.* **757**, 701–746.

GOTO, S., SAITO, Y. & KAWAHARA, G. 2017 Hierarchy of antiparallel vortex tubes in spatially periodic turbulence at high Reynolds numbers. *Phys. Rev. Fluids* **2** (6), 064603.

GOTTLIEB, S., SHU, C.W. & TADMOR, E. 2001 Strong stability-preserving high-order time discretization methods. *SIAM Rev.* **43** (1), 89–112.

GRIFFIN, K.P., FU, L. & MOIN, P. 2021 Velocity transformation for compressible wall-bounded turbulent flows with and without heat transfer. *Proc. Natl Acad. Sci.* **118** (34), e2111144118.

GUEZENNEC, Y., STRETCH, D. & KIM, J. 1990 The structure of turbulent channel flow with passive scalar transport. *Studying Turbulence Using Numerical Simulation Databases. 3: Proceedings of the 1990 Summer Program, Centre for Turbulence Research*, pp. 127–138. Stanford University.

GUPTA, V., MADHUSUDANAN, A., WAN, M., ILLINGWORTH, S.J. & JUNIPER, M.P. 2021 Linear-model-based estimation in wall turbulence: improved stochastic forcing and eddy viscosity terms. *J. Fluid Mech.* **925**, A18.

HIRAI, R., PECNIK, R. & KAWAI, S. 2021 Effects of the semi-local Reynolds number in scaling turbulent statistics for wall heated/cooled supersonic turbulent boundary layers. *Phys. Rev. Fluids* **6** (12), 124603.

HU, R., YANG, X.I.A. & ZHENG, X. 2020 Wall-attached and wall-detached eddies in wall-bounded turbulent flows. *J. Fluid Mech.* **885**, A30.

HUANG, J., DUAN, L. & CHOUDHARI, M.M. 2022 Direct numerical simulation of hypersonic turbulent boundary layers: effect of spatial evolution and Reynolds number. *J. Fluid Mech.* **937**, A3.

HUANG, P.G., COLEMAN, G.N. & BRADSHAW, P. 1995 Compressible turbulent channel flows: DNS results and modelling. *J. Fluid Mech.* **305**, 185–218.

HUTCHINS, N. & MARUSIC, I. 2007 Evidence of very long meandering features in the logarithmic region of turbulent boundary layers. *J. Fluid Mech.* **579**, 1–28.

HWANG, J., LEE, J. & SUNG, H. 2020 Statistical behaviour of self-similar structures in canonical wall turbulence. *J. Fluid Mech.* **905**, A6.

HWANG, J. & SUNG, H.J. 2018 Wall-attached structures of velocity fluctuations in a turbulent boundary layer. *J. Fluid Mech.* **856**, 958–983.

HWANG, Y. 2013 Near-wall turbulent fluctuations in the absence of wide outer motions. *J. Fluid Mech.* **723** (5), 264–288.

HWANG, Y. 2015 Statistical structure of self-sustaining attached eddies in turbulent channel flow. *J. Fluid Mech.* **767**, 254–289.

KIM, J., MOIN, P. & MOSER, R. 1987 Turbulence statistics in fully developed channel flow at low Reynolds number. *J. Fluid Mech.* **177** (177), 133–166.

KLINE, S.J., REYNOLDS, W.C., SCHRAUB, F.A. & RUNSTADLER, P.W. 1967 The structure of turbulent boundary layers. *J. Fluid Mech.* **30** (4), 741–773.

LEE, M. & MOSER, R.D. 2019 Spectral analysis of the budget equation in turbulent channel flows at high Reynolds number. *J. Fluid Mech.* **860**, 886–938.

LI, W., FAN, Y., MODESTI, D. & CHENG, C. 2019 Decomposition of the mean skin-friction drag in compressible turbulent channel flows. *J. Fluid Mech.* **875**, 101–123.

LOZANO-DURÁN, A. & BAE, H.J. 2019 Characteristic scales of Townsend's wall-attached eddies. *J. Fluid Mech.* **868**, 698–725.

LOZANO-DURÁN, A., CONSTANTINOU, N.C., NIKOLAIDIS, M. & KARP, M. 2021 Cause-and-effect of linear mechanisms sustaining wall turbulence. *J. Fluid Mech.* **914**, A8.

LOZANO-DURÁN, A., FLORES, O. & JIMÉNEZ, J. 2012 The three-dimensional structure of momentum transfer in turbulent channels. *J. Fluid Mech.* **694**, 100–130.

MARUSIC, I., BAARS, W.J. & HUTCHINS, N. 2017 Scaling of the streamwise turbulence intensity in the context of inner-outer interactions in wall turbulence. *Phys. Rev. Fluids* **2** (10), 100502.

MARUSIC, I. & MONTY, J.P. 2019 Attached eddy model of wall turbulence. *Annu. Rev. Fluid Mech.* **51**, 49–74.

MATHIS, R., HUTCHINS, N. & MARUSIC, I. 2011 A predictive inner–outer model for streamwise turbulence statistics in wall-bounded flows. *J. Fluid Mech.* **681**, 537–566.

MODESTI, D. & PIROZZOLI, S. 2016 Reynolds and Mach number effects in compressible turbulent channel flow. *Intl J. Heat Fluid Flow* **59**, 33–49.

MORKOVIN, M.V. 1962 Effects of compressibility on turbulent flows. *Mécanique de la Turbul.* **367** (380), 26.

PASSIATORE, D., SCIACOVELLI, L., CINNELLA, P. & PASCAZIO, G. 2022 Thermochemical non-equilibrium effects in turbulent hypersonic boundary layers. *J. Fluid Mech.* **941**, A21.

PATEL, A., PEETERS, J.W., BOERSMA, B.J. & PECNIK, R. 2015 Semi-local scaling and turbulence modulation in variable property turbulent channel flows. *Phys. Fluids* **27** (9), 095101.

PERRY, A.E. & CHONG, M.S. 1982 On the mechanism of wall turbulence. *J. Fluid Mech.* **119** (119), 173–217.

PERRY, A.E. & MARUSIC, I. 1995 A wall-wake model for the turbulence structure of boundary layers. Part 1. Extension of the attached eddy hypothesis. *J. Fluid Mech.* **298** (298), 361–388.

PIROZZOLI, S. & BERNARDINI, M. 2011 Turbulence in supersonic boundary layers at moderate Reynolds number. *J. Fluid Mech.* **688**, 120–168.

PIROZZOLI, S., BERNARDINI, M. & ORLANDI, P. 2016 Passive scalars in turbulent channel flow at high Reynolds number. *J. Fluid Mech.* **788**, 614–639.

RUBESIN, M.W. 1990 Extra compressibility terms for Favre-averaged two-equation models of inhomogeneous turbulent flows. *NASA Tech. Rep.* CR-177556.

SCIACOVELLI, L., CINNELLA, P. & GLOERFELT, X. 2017 Direct numerical simulations of supersonic turbulent channel flows of dense gases. *J. Fluid Mech.* **821**, 153–199.

SMITS, A.J., HULTMARK, M., LEE, M., PIROZZOLI, S. & WU, X. 2021 Reynolds stress scaling in the near-wall region of wall-bounded flows. *J. Fluid Mech.* **926**, A31.

TINNEY, C.E., COIFFET, F., DELVILLE, J., HALL, A.M., JORDAN, P. & GLAUSER, M.N. 2006 On spectral linear stochastic estimation. *Exp. Fluids* **41** (5), 763–775.

TOWNSEND, A.A. 1976 *The Structure of Turbulent Shear Flow*, 2nd edn. Cambridge University Press.

TSUJI, Y., MARUSIC, I. & JOHANSSON, A.V. 2016 Amplitude modulation of pressure in turbulent boundary layer. *Intl J. Heat Fluid Flow* **61**, 2–11.

YANG, X.I.A., MARUSIC, I. & MENEVEAU, C. 2016 Moment generating functions and scaling laws in the inertial layer of turbulent wall-bounded flows. *J. Fluid Mech.* **791**, R2.

YAO, J. & HUSSAIN, F. 2020 Turbulence statistics and coherent structures in compressible channel flow. *Phys. Rev. Fluids* **5** (8), 084603.

YOON, M., HWANG, J., YANG, J. & SUNG, H.J. 2020 Wall-attached structures of streamwise velocity fluctuations in an adverse-pressure-gradient turbulent boundary layer. *J. Fluid Mech.* **885**, A12.

YU, M. & XU, C. 2021 Compressibility effects on hypersonic turbulent channel flow with cold walls. *Phys. Fluids* **33** (7), 075106.

YU, M., XU, C., CHEN, J.Q., LIU, P.X., FU, Y.L. & YUAN, X.X. 2022 Spectral decomposition of wall-attached/detached eddies in compressible and incompressible turbulent channel flows. *Phys. Rev. Fluids* **7** (5), 054607.

YUAN, X., TONG, F., LI, W., CHEN, J. & DONG, S. 2022 Wall-attached temperature structures in supersonic turbulent boundary layers. *Phys. Fluids* **34** (11), 115116.

ZHANG, Y.S., BI, W.T., HUSSAIN, F. & SHE, Z.S. 2014 A generalized Reynolds analogy for compressible wall-bounded turbulent flows. *J. Fluid Mech.* **739**, 392–420.